Geosci. Model Dev. Discuss., 8, 3147–3196, 2015
www.geosci-model-dev-discuss.net/8/3147/2015/
doi:10.5194/gmdd-8-3147-2015

Geoscientific Model Development Discussions
Open Access

The Yale Interactive terrestrial Biosphere model: description, evaluation and implementation into NASA GISS ModelE2

X. Yue and N. Unger

School of Forestry and Environment Studies, Yale University, New Haven, Connecticut 06511, USA

Received: 24 March 2015 – Accepted: 26 March 2015 – Published: 10 April 2015

Correspondence to: X. Yue (xuyueseas@gmail.com)

Published by Copernicus Publications on behalf of the European Geosciences Union.

Abstract

The land biosphere, atmospheric chemistry and climate are inextricably interconnected. We describe the **Y**ale **I**nteractive terrestrial **Bio**s**p**here (YIBs) model, a land carbon cycle model that has been developed for coupling to the NASA Goddard Institute for Space Studies (GISS) ModelE2 global chemistry–climate model. The YIBs model adapts routines from the mature TRIFFID and CASA models to simulate interactive carbon assimilation, allocation, and autotrophic and heterotrophic respiration. Dynamic daily leaf area index is simulated based on carbon allocation and temperature- and drought-dependent prognostic phenology. YIBs incorporates a semi-mechanistic ozone vegetation damage scheme. Here, we validate the present day YIBs land carbon fluxes for three increasingly complex configurations: (i) off-line local site-level (ii) off-line global forced with WFDEI (WATCH Forcing Data methodology applied to ERA-Interim data) meteorology (iii) on-line coupled to the NASA ModelE2 (NASA ModelE2-YIBs). Off-line YIBs has hourly and on-line YIBs has half-hourly temporal resolution. The large observational database used for validation includes carbon fluxes from 145 flux tower sites and multiple satellite products. At the site level, YIBs simulates reasonable seasonality (correlation coefficient $R > 0.8$) of gross primary productivity (GPP) at 121 out of 145 sites with biases in magnitude ranging from −19 to 7 % depending on plant function type. On the global scale, the off-line model simulates an annual GPP of 125 ± 3 petagrams of carbon (Pg C) and net ecosystem exchange (NEE) of -2.5 ± 0.7 Pg C for 1982–2011, with seasonality and spatial distribution consistent with the satellite observations. We assess present day global ozone vegetation damage using the off-line YIBs configuration. Ozone damage reduces global GPP by 2–5 % annually with regional extremes of 4–10 % in East Asia. The on-line model simulates annual GPP of 123 ± 1 Pg C and NEE of -2.7 ± 0.7 Pg C. NASA ModelE2-YIBs is a useful new tool to investigate coupled interactions between the land carbon cycle, atmospheric chemistry, and climate change.

GMDD
8, 3147–3196, 2015

1 Introduction

The terrestrial biosphere interacts with the atmosphere through the exchanges of energy, carbon, reactive gases, water, and momentum fluxes. Forest ecosystems absorb an estimated 120 petagrams of carbon (Pg C) per year from the atmosphere (Beer et al., 2010) and mitigate about one quarter of the anthropogenic carbon dioxide (CO_2) emissions (Friedlingstein et al., 2014). This carbon assimilation is sensitive to human-caused perturbations including climate change and land use change (Zhao and Running, 2010; Houghton et al., 2012), and is affected by atmospheric pollutants such as ozone and aerosols (Sitch et al., 2007; Mercado et al., 2009). Over the past 2–3 decades, a number of terrestrial biosphere models have been developed as tools to quantify the present-day global carbon budget in conjunction with available but sparse observations (e.g., Jung et al., 2009), to understand the relationships between terrestrial biospheric fluxes and environmental conditions (e.g., Zeng et al., 2005), to attribute drivers of trends in the carbon cycle during the anthropogenic era (e.g., Sitch et al., 2015), and to project future changes in the land biosphere and the consequences for regional and global climate change (e.g., Friedlingstein et al., 2006).

Emerging research identifies climatically-relevant interactions between the land biosphere and atmospheric chemistry (e.g., Huntingford et al., 2011). For instance, stomatal uptake is an important sink of tropospheric ozone (Val Martin et al., 2014), but damages photosynthesis, reduces plant growth and biomass accumulation, limits crop yields, and affects stomatal control over plant transpiration of water vapor between the leaf surface and atmosphere (Ainsworth, 2012; Hollaway et al., 2012). The indirect CO_2 radiative forcing due to the vegetation damage effects of anthropogenic ozone increases since the industrial revolution may be as large as $+0.4\,W\,m^{-2}$ (Sitch et al., 2007), which is 25 % of the magnitude of the direct CO_2 radiative forcing over the same period, and of similar magnitude to the direct ozone radiative forcing. Atmospheric oxidation of biogenic volatile organic compound (BVOC) emissions affects surface air quality and exerts additional regional and global chemical climate forcings (Scott et al.,

GMDD
8, 3147–3196, 2015

2014; Unger, 2014a, b). Fine mode atmospheric pollution particles affect the land biosphere by changing the physical climate state and through diffuse radiation fertilization (Mercado et al., 2009; Mahowald, 2011). Land plant phenology has experienced substantial changes in the last few decades (Keenan et al., 2014), possibly influencing both ozone deposition and BVOC emissions through the extension of growing seasons. These coupled interactions are often not adequately represented in current generation land biosphere models or global chemistry–climate models.

In this study, we present the description and present-day evaluation of the Yale Interactive terrestrial Biosphere model (YIBs) in three configurations: (i) off-line local site-level (ii) off-line global forced with WFDEI (WATCH Forcing Data methodology applied to ERA-Interim data) meteorology (iii) on-line coupled to the latest frozen version of the NASA GISS ModelE2 (Schmidt et al., 2014). The global climate model represents atmospheric gas-phase and aerosol chemistry, cloud, radiation, and land surface processes, and has been widely used for studies of atmospheric components, climate change, and their interactions (Schmidt et al., 2006; Koch et al., 2011; Unger, 2011; Shindell et al., 2013; Miller et al., 2014). The goal of this study is to evaluate the YIBs land carbon cycle fluxes and vegetation behavior for the present day. The impacts of the updated vegetation scheme on the chemistry and climate simulations in NASA ModelE2 will be addressed in other on-going research. Section 2 describes the observational datasets used to evaluate YIBs land carbon cycle performance. Section 3 describes physical parameterizations of the vegetation model. Section 4 explains the model set up and simulations in three configurations. Section 5 presents the results of the model evaluation and Sect. 6 summarizes the model performance.

GMDD
8, 3147–3196, 2015

2 Observational datasets for validation

2.1 Site-level measurements

To validate the YIBs model, we use eddy covariance measurements from 145 flux tower sites (Fig. 1), which are collected by the North American Carbon Program (Schaefer et al., 2012) and the FLUXNET (http://fluxnet.ornl.gov) network. Among these sites, 138 are located in the Northern Hemisphere, with 74 in Europe, 38 in US, and 24 in Canada (Table S1 in the Supplement). Sites on other continents are limited. Most of the sites have one dominant plant function type (PFT), including 54 sites of evergreen needleleaf forests (ENF), 20 deciduous broadleaf forests (DBF), 9 evergreen broadleaf forests (EBF), 28 grasslands, 18 shrublands, and 16 croplands. We attribute sites with mixed forest to the ENF as these sites are usually at high latitudes. Each site dataset provides hourly or half-hourly measurements of carbon fluxes, including gross primary productivity (GPP) and net ecosystem exchange (NEE), and CO_2 concentrations and meteorological variables, such as surface air temperature, relative humidity, wind speed, and shortwave radiation.

2.2 Global measurements

We use global tree height, leaf area index (LAI), GPP, net primary productivity (NPP), and phenology datasets to validate the vegetation model. Canopy height is retrieved using 2005 remote sensing data from the Geoscience Laser Altimeter System (GLAS) aboard ICESat satellite (Simard et al., 2011). LAI measurements for 1982–2011 are derived using the Normalized Difference Vegetation Index (NDVI) from Global Inventory Modeling and Mapping Studies (GIMMS) (Zhu et al., 2013). Global GPP observations of 1982–2011 are estimated based on the upscaling of FLUXNET eddy covariance data with a biosphere model (Jung et al., 2009). As a comparison, we also use GPP observations of 1982–2008 derived based on FLUXNET, satellite, and meteorological observations (Jung et al., 2011), which is about 10 % lower than that of Jung

GMDD
8, 3147–3196, 2015

et al. (2009). The NPP for 2000–2011 is derived using remote sensing data from Moderate Resolution Imaging Spectroradiometer (MODIS) (Zhao et al., 2005). We use the global retrieval of greenness onset derived from the Advanced Very High Resolution Radiometer (AVHRR) and the MODIS data from 1982 to 2011 (Zhang et al., 2014). All datasets are interpolated to the $1^{\circ} \times 1^{\circ}$ off-line model resolution for comparisons.

3 YIBs model description

Previously, we presented and evaluated an off-line regional version of YIBs that was applied to assess ozone damage effects on GPP in the US (Yue and Unger, 2014); and an on-line global version of YIBs that was used to investigate BVOC–chemistry–climate interactions (Unger, 2013; Unger and Yue, 2014). Here, we describe the recent updated functionalities of the YIBs model that now represents the complete land carbon cycle: interactive carbon assimilation, allocation, autotrophic and heterotrophic respiration, and dynamic tree growth (changes in both height and LAI).

3.1 Vegetation biophysics

YIBs calculates carbon uptake for 9 plant functional types (PFTs): tundra, C_3 / C_4 grass, shrubland, DBF, ENF, EBF, and C_3 / C_4 cropland (Table 1). In the gridded large-scale model applications, each model PFT fraction in the vegetated part of each grid cell represents a single canopy. The vegetation biophysics simulates C_3 and C_4 photosynthesis with the well-established Michealis-Menten enzyme-kinetics scheme (Farquhar et al., 1980; von Caemmerer and Farquhar, 1981) and the stomatal conductance model of Ball and Berry (Collatz et al., 1991). The total leaf photosynthesis (A_{tot}, $\mu mol\, m^{-2}$ [leaf] s^{-1}) is limited by one of three processes: (i) the capacity of the ribulose 1,5-bisphosphate (RuBP) carboxylase-oxygenase enzyme (Rubisco) to catalyze carbon fixation (J_c), (ii) the capacity of the Calvin cycle and the thylakoid reactions to regenerate RuBP supported by electron transport (J_e), (iii) the capacity of starch and

GMDD
8, 3147–3196, 2015

sucrose synthesis to regenerate inorganic phosphate for photo- phosphorylation in C_3 plants and phosphoenolpyruvate (PEP) in C_4 plants (J_s).

$$A_{tot} = \min(J_c, J_e, J_s) \quad (1)$$

The J_c, J_e, and J_s are parameterized as functions of environmental variables (e.g. temperature, radiation, and CO_2 concentrations) and the maximum carboxylation capacity (V_{cmax}, $\mu mol\, m^{-2}\, s^{-1}$) (Farquhar et al., 1980):

$$J_c = \begin{cases} V_{cmax}\left(\frac{c_i - \Gamma_*}{c_i + K_c(1+O_i/K_o)}\right) & \text{for } C_3 \text{ plant} \\ V_{cmax} & \text{for } C_4 \text{ plant} \end{cases} \quad (2)$$

$$J_e = \begin{cases} a_{leaf} \cdot PAR \cdot \alpha \cdot \left(\frac{c_i - \Gamma_*}{c_i + 2\Gamma_*}\right) & \text{for } C_3 \text{ plant} \\ a_{leaf} \cdot PAR \cdot \alpha & \text{for } C_4 \text{ plant} \end{cases} \quad (3)$$

$$J_s = \begin{cases} 0.5 V_{cmax} & \text{for } C_3 \text{ plant} \\ K_s \cdot V_{cmax} \cdot \frac{c_i}{P_s} & \text{for } C_4 \text{ plant} \end{cases} \quad (4)$$

where c_i and O_i are the leaf internal partial pressure (Pa) of CO_2 and oxygen, Γ_* (Pa) is the CO_2 compensation point, K_c and K_o (Pa) are Michaelis–Menten parameters for the carboxylation and oxygenation of rubisco. The parameters K_c, K_o, and Γ_* vary with temperature according to a Q_{10} function. PAR ($\mu mol\, m^{-2}\, s^{-1}$) is the incident photosynthetically active radiation, a_{leaf} is leaf-specific light absorbance, and α is intrinsic quantum efficiency. P_s is the ambient pressure and K_s is a constant set to 4000 following Oleson et al. (2010). V_{cmax} is a function of the optimal V_{cmax} at 25 °C (V_{cmax25}) based on a Q_{10} function.

Net carbon assimilation (A_{net}) of leaf is given by:

$$A_{net} = A_{tot} - R_d \quad (5)$$

GMDD
8, 3147–3196, 2015

where R_d is the rate of dark respiration set to 0.011 V_{cmax} for C_3 plants (Farquhar et al., 1980) and 0.025 V_{cmax} for C_4 plants (Clark et al., 2011). The stomatal conductance of water vapor (g_s in mol [H_2O] m^{-2} s^{-1}) is dependent on net photosynthesis:

$$g_s = m\frac{A_{net} \cdot RH}{c_s} + b \quad (6)$$

where m and b are the slope and intercept derived from empirical fitting to the Ball and Berry stomatal conductance equations, RH is relative humidity, and c_s is the CO_2 concentration at the leaf surface. In the model, the slope m is influenced by water stress, so that drought decreases photosynthesis by affecting stomatal conductance. Appropriate photosynthesis parameters for different vegetation types are taken from Friend and Kiang (2005) and the Community Land Model (Oleson et al., 2010) with updates from Bonan et al. (2011) (Table 1).

The coupled equation system of photosynthesis, stomatal conductance and CO_2 diffusive flux transport equations form a cubic in c_i that is solved analytically (Baldocchi, 1994). A simplified but realistic representation of soil water stress β is included in the vegetation biophysics following the approach of Porporato et al. (2001). The algorithm reflects the relationship between soil water amount and the extent of stomatal closure ranging from no water stress to the soil moisture stress onset point (s^*) through to the wilting point (s_{wilt}). Stomatal conductance is reduced linearly between the PFT-specific values of s^* and s_{wilt} based on the climate model's soil water volumetric saturation in 6 soil layers (Unger et al., 2013).

The canopy radiative transfer scheme divides the canopy into an adaptive number of layers (typically 2–16) for light stratification. Each canopy layer distinguishes sunlit and shaded portions of leaves, so that the direct and diffuse photosynthetically active radiation (PAR) is used for carbon assimilation respectively (Spitters, 1986). The leaf

GMDD
8, 3147–3196, 2015

photosynthesis is then integrated over all canopy layers to generate the GPP:

$$\mathrm{GPP} = \int_0^{\mathrm{LAI}} A_{\mathrm{tot}} \mathrm{d}L \tag{7}$$

3.2 Leaf phenology

Phenology determines the annual cycle of LAI. Plant phenology is generally controlled by temperature, water availability, and photoperiod (Richardson et al., 2013). For deciduous trees, the timing of budburst is sensitive to temperature (Vitasse et al., 2009) and the autumn senescence is related to both temperature and photoperiod (Delpierre et al., 2009). For small trees and grasses, such as tundra, savanna, and shrubland, phenology is controlled by temperature and/or soil moisture, depending on the species type and locations of the vegetation (Delbart and Picard, 2007; Liu et al., 2013). In the YIBs model, leaf phenology is updated on a daily basis. For the YIBs model, we have extended the phenology scheme proposed by Kim and Wang (2005), based on long-term measurements of leaf phenology at 5 US sites (Yue et al., 2015a, hereinafter Y2015) and GPP at the 145 flux tower sties. A summary of the phenological parameters adopted is listed in Table 2.

3.2.1 Deciduous broadleaf forest (DBF)

We predict spring phenology of DBF using the cumulative thermal summation (White et al., 1997). The accumulative growing degree day (GDD) is calculated for the nth day from winter solstice if the 10 day average air temperature T_{10} is higher than a base temperature T_{b}:

$$\mathrm{GDD} = \sum_{i=1}^{n} \max(T_{10} - T_{\mathrm{b}}, 0) \tag{8}$$

GMDD
8, 3147–3196, 2015

Here T_b is set to 5 °C as that in Murray et al. (1989). The onset of greenness is triggered if the GDD exceeds a threshold value G_b and a temperature-dependent phenological factor f_T is calculated as follows:

$$f_T = \begin{cases} \min\left(1, \frac{\mathrm{GDD}-G_b}{L_g}\right), & \text{if GDD} \geq G_b \\ 0, & \text{otherwise} \end{cases} \quad (9)$$

Following Murray et al. (1989), the threshold $G_b = a + b\exp(r \cdot \mathrm{NCD})$ is dependent on the number of chill days (NCD), which is calculated as the total days with < 5 °C from winter solstice.

The autumn phenology is more uncertain than budburst because it is affected by both temperature and photoperiod (White et al., 1997; Delpierre et al., 2009). For the temperature dependent phenology, we adopted the cumulative cold summation method (Dufrene et al., 2005; Richardson et al., 2006), which calculates the accumulative falling degree day (FDD) for the mth day from summer solstice as follows,

$$\mathrm{FDD} = \sum_{i=1}^{m} \min(T_{10} - T_s, 0) \quad (10)$$

where T_s is 20 °C as that in Dufrene et al. (2005). Similar to the budburst process, we determine autumn phenological factor based on a fixed threshold F_s:

$$f_T = \begin{cases} \max\left(0, 1 + \frac{\mathrm{FDD}-F_s}{L_f}\right), & \text{if FDD} \leq F_s \\ 1, & \text{otherwise} \end{cases} \quad (11)$$

In addition, we assume photoperiod regulates leaf senescence as follows,

$$f_P = \begin{cases} \max\left(0, \frac{P-P_i}{P_x-P_i}\right), & \text{if } P \leq P_x \\ 1, & \text{otherwise} \end{cases} \quad (12)$$

GMDD
8, 3147–3196, 2015

where f_P is the photoperiod-limited phenology. P is daylength in minutes. P_i and P_x are the lower and upper limits of daylength for the period of leaf fall. Finally, the autumn phenology of DBF is determined as the product of f_T (Eq. 11) and f_P (Eq. 12). Both the spring and autumn phenology schemes have been evaluated with extensive ground records over the US in Y2015.

3.2.2 Shrubland

Shrub phenology is sensitive to temperature and/or water availability. We calculate correlation coefficients between observed GPP and soil meteorology at 18 shrub sites (Fig. 2). For 10 sites with annual mean soil temperature $< 9\,^{\circ}C$, the GPP-temperature correlations are close to 1 while the GPP-moisture correlations are all negative (Fig. 2a), suggesting that temperature is the dominant phenological driver for these plants. In contrast, for 8 sites with average soil temperature $> 14\,^{\circ}C$, GPP-moisture correlations are positive and usually higher than the GPP-temperature correlations, indicating that phenology is primarily regulated by water availability at climatologically warm areas. The wide temperature gap (9–14 $^{\circ}C$) is due to the limit in the availability of shrub sites. Here, we select a tentative threshold of $12\,^{\circ}C$ to distinguish cold and drought species. We also try to identify phenological drivers based on soil moisture thresholds but find that both temperature- and drought-dependent phenology may occur at moderately dry conditions (Fig. 2b).

In the model, we apply the temperature-dependent phenology f_T for shrubland, if the site has annual mean soil temperature $< 12\,^{\circ}C$. We use the same f_T as that for DBF (Eqs. 9 and 11), due to the lack of long-term phenology measurements at the shrub sites. However, if the soil temperature is $> 12\,^{\circ}C$, the plant growth is controlled by drought-limit phenology f_D instead:

$$f_D = \begin{cases} \max\left(0, \frac{\beta_{10}-\beta_{\min}}{\beta_{\max}-\beta_{\min}}\right), & \text{if } \beta_{10} \le \beta_{\max} \\ 1, & \text{otherwise} \end{cases} \quad (13)$$

GMDD
8, 3147–3196, 2015

where β_{10} is 10 day average water stress calculated based on soil moisture, soil ice fraction, and root fraction of each soil layer (Porporato et al., 2001). The value of β_{10} changes from 0 to 1, with lower value indicating drier soil. Two thresholds, β_{max} and β_{min}, represent the upper and lower thresholds that trigger the drought limit for woody species. The values of these thresholds are set to $\beta_{max} = 1$ and $\beta_{min} = 0.4$ so that the predicted phenology has the maximum correlations with the observed GPP seasonality (Fig. S1a in the Supplement).

3.2.3 Grassland

In the model, we consider temperature-dependent phenology for grassland based on soil temperature (ST) accumulation (White et al., 1997):

$$\mathrm{SGDD} = \sum_{i=1}^{n} \max\left(\mathrm{ST}_{10} - \mathrm{ST}_{\mathrm{b}}, 0\right) \tag{14}$$

where ST_{10} is 10 day average soil temperature and $\mathrm{ST}_{\mathrm{b}} = 0\,^{\circ}\mathrm{C}$. Similar to DBF, the onset of grass greenness is triggered if SGDD is higher than a threshold value SG_{b}:

$$f_T = \begin{cases} \min\left(1, \frac{\mathrm{SGDD}-\mathrm{SG_b}}{\mathrm{SL_g}}\right), & \text{if SGDD} \geq \mathrm{SG_b} \\ 0, & \text{otherwise} \end{cases} \tag{15}$$

where SL_{g} determines the grow length of grass. Both SG_{b} and SL_{g} are calibrated based on observed GPP seasonality at FLUXNET sites (Table 2). Grass phenology at warm sites is also sensitive to water stress (Fig. 2c). We apply the same drought-limit phenology f_{D} as shrubland (Eq. 13) for grassland but with calibrated threshold $\beta_{max} = 0.9$ and $\beta_{min} = 0.3$ (Fig. S1b). Different from shrubland whose phenology is dominated by drought when $\mathrm{ST} > 12\,^{\circ}\mathrm{C}$ (Fig. 2a), grassland phenology is jointly affected by temperature and soil moisture (Fig. 2c). As a result, the final phenology for grassland at warm regions is the minimum of f_T and f_{D}.

GMDD
8, 3147–3196, 2015

3.2.4 Other PFTs

YIBs considers two evergreen PFTs, ENF at high latitudes and EBF in tropical areas. Observations do suggest that evergreen trees experience seasonal changes in LAI, following temperature variations and/or water availability (Doughty and Goulden, 2008; Schuster et al., 2014). However, due to the large uncertainty of evergreen phenology, we set a constant phenology factor of 1.0 for these species, following the approach adopted in other process-based vegetation models (Bonan et al., 2003; Sitch et al., 2003). We implement a parameterization for the impact of cold temperature (frost hardening) on the maximum carboxylation capacity (V_{cmax}) so as to reduce cold injury for ENF during winter (Hanninen and Kramer, 2007). EBF may experience reduced photosynthesis during the dry season through the effects of water stress on stomatal conductance (Jones et al., 2014).

Crop phenology depends on planting and harvesting dates. In YIBs, we apply a global dataset of crop planting and harvesting dates (Sacks et al., 2010; Unger et al., 2013). Crop budburst occurs at the plant date and the crop continues to grow for a period of 30 days until reaching full maturity ($f = 1$). The crop leaves begin to fall 15 days prior to the harvest date, after which phenology is set to 0. A similar treatment has been adopted in Community Land Model (CLM) (Bonan et al., 2003). Thus, crop productivity but not crop phenology is sensitive to the imposed meteorological forcings.

3.3 Carbon allocation

We adopt the autotrophic respiration and carbon allocation scheme applied in the dynamic global vegetation model (DGVM) TRIFFID (Cox, 2001; Clark et al., 2011). On a daily basis, the plant LAI is updated as follows:

$$\mathrm{LAI} = f \cdot \mathrm{LAI_b} \tag{16}$$

where f is the phenological factor, and $\mathrm{LAI_b}$ is the biomass-balanced (or available maximum) LAI related to tree height. $\mathrm{LAI_b}$ is dependent on the vegetation carbon content

GMDD
8, 3147–3196, 2015

C_{veg}, which is the sum of carbon from leaf (C_l), root (C_r), and stem (C_w):

$$C_{veg} = C_l + C_r + C_w \tag{17}$$

where each carbon component is a function of LAI_b:

$$C_l = \sigma_l \cdot LAI \tag{18a}$$

$$C_r = \sigma_l \cdot LAI_b \tag{18b}$$

$$C_w = a_{wl} \cdot LAI_b^{b_{wl}} \tag{18c}$$

here σ_l is the specific leaf carbon density. a_{wl} and b_{wl} are PFT-specified allometric parameters (Table 1). The vegetation carbon content C_{veg} is updated every 10 days based on the carbon balance of assimilation, respiration, and litter fall.

$$\frac{dC_{veg}}{dt} = (1 - \lambda) \cdot NPP - \Lambda_l \tag{19}$$

The net primary productivity (NPP) is the net carbon uptake:

$$NPP = GPP - R_a \tag{20}$$

here GPP is the total photosynthesis rate integrated over LAI. Autotrophic respiration (R_a) is split into maintenance (R_{am}) and growth respiration (R_{ag}) (Clark et al., 2011):

$$R_a = R_{am} + R_{ag} \tag{21}$$

The maintenance respiration is calculated based on nitrogen content in leaf (N_l), root (N_r), and stem (N_w) as follows,

$$R_{am} = 0.012 R_{dc} \left(\beta + \frac{N_r + N_w}{N_l} \right) \tag{22}$$

GMDD
8, 3147–3196, 2015

where R_{dc} is the dark respiration of leaf, which is dependent on leaf temperature and is integrated over whole canopy LAI. The factor of 0.012 is the unit conversion from $\mathrm{mol\,CO_2\,m^{-2}\,s^{-1}}$ to $\mathrm{kg\,C\,m^{-2}\,s^{-1}}$ and β is water stress representing soil water availability. The nitrogen contents are given by:

$$N_l = n_0 \cdot C_l \tag{23a}$$

$$N_r = n_{rl} \cdot n_0 \cdot C_r \tag{23b}$$

$$N_w = n_{wl} \cdot n_0 \cdot C_w \tag{23c}$$

here n_0 is leaf nitrogen concentration, n_{rl} and n_{wl} are ratios of nitrogen concentrations of root and stem to leaves. We adopt the same values of n_0, n_{rl} and n_{wl} as that of TRIFFID model (Table 1) except that n_{rl} is set to 0.5 following observations of deciduous trees by Sugiura and Tateno (2011). The growth respiration is dependent on the residual between GPP and R_{am} based on a ratio r_g set to 0.2 for all PFTs (Knorr, 2000):

$$R_{ag} = r_g \cdot (\mathrm{GPP} - R_{am}) \tag{24}$$

The λ in Eq. (19) is a partitioning coefficient determining the fraction of NPP used for spreading:

$$\lambda = \begin{cases} 1, & \text{if } \mathrm{LAI_b} > \mathrm{LAI_{max}} \\ \frac{\mathrm{LAI_b} - \mathrm{LAI_{min}}}{\mathrm{LAI_{max}} - \mathrm{LAI_{min}}}, & \text{if } \mathrm{LAI_{min}} \le \mathrm{LAI_b} \le \mathrm{LAI_{max}} \\ 0, & \text{if } \mathrm{LAI_b} < \mathrm{LAI_{min}} \end{cases} \tag{25}$$

where $\mathrm{LAI_{min}}$ and $\mathrm{LAI_{max}}$ are minimum and maximum LAI values for a specific vegetation type (Table 1). The litter fall rate Λ_l in Eq. (19) consists of contributions from leaf, root, and stem as follows,

$$\Lambda_l = \gamma_l \cdot C_l + \gamma_r \cdot C_r + \gamma_w \cdot C_w \tag{26}$$

GMDD
8, 3147–3196, 2015

here γ_l, γ_r, and γ_w are turnover rate (yr^{-1}) for leaf, root, and stem carbon respectively. The leaf turnover rate is calculated based on the phenology change every day. The root and stem turnover rates are PFT-specific constants (Table 1), derived based on the meta-analysis by Gill and Jackson (2000) for root and Stephenson and van Mantgem (2005) for stem.

3.4 Soil respiration

The soil respiration scheme is developed based on the Carnegie-Ames-Stanford Approach (CASA) model (Schaefer et al., 2008), which considers carbon flows among 12 biogeochemical pools. Three live pools, including leaf C_l, root C_r, and wood C_w, contain biomass carbon assimilated from photosynthesis. Litterfall from live pools decomposes and transits in nine dead pools, which consist of one coarse woody debris (CWD) pool, three surface pools, and five soil pools. The CWD pool is composed of dead trees and woody roots. Both surface and soil have identical pools, namely structural, metabolic, and microbial pools, which are distinguished by the content and functions. The structural pool contains lignin, the metabolic pool contains labile substrates, and the microbial pool represents microbial populations. The remaining two soil pools, the slow and passive pools, consist of organic material that decays slowly. The full list of carbon flows among different pools has been illustrated by Schaefer et al. (2008) (c.f. their Fig. 1).

When carbon transfers from pool j to pool i, the carbon loss of pool j is:

$$L_{j2i} = f_{j2i} k_j C_j \tag{27}$$

where C_j is the carbon in pool j, k_j is the total carbon loss rate of pool j, and f_{j2i} is the fraction of carbon lost from pool j transferred to pool i. The coefficient k_j is dependent on soil temperature, moisture, and texture. Meanwhile, the carbon gain of pool i is:

$$G_{j2i} = e_{j2i} \cdot L_{j2i} = e_{j2i} f_{j2i} k_j C_j \tag{28}$$

GMDD
8, 3147–3196, 2015

where e_{j2i} is the ratio of carbon received by pool i to the total carbon transferred from pool j. The rest of the transferred carbon is lost due to heterotrophic respiration:

$$R_{j2i} = (1 - e_{j2i}) \cdot L_{j2i} \tag{29}$$

As a result, the carbon in the ith pool is calculated as

$$\frac{dC_i}{dt} = \sum_{j=1}^{n} G_{j2i} - \sum_{k=1}^{m} L_{i2k} \tag{30}$$

The total heterotrophic respiration (R_h) is the summation of R_{j2i} for all pair pools where carbon transitions occur. The total soil carbon is the summation of carbon for all dead pools:

$$C_{soil} = \sum_{i=1}^{9} C_i \tag{31}$$

The net ecosystem productivity (NEP) is calculated as

$$NEP = -NEE = NPP - R_h = GPP - R_a - R_h \tag{32}$$

where NEE is the net ecosystem exchange, representing net carbon flow from land to atmosphere. YIBs does not yet account for NEE perturbations due to dynamic disturbance.

3.5 Ozone vegetation damage effects

We apply the semi-mechanistic parameterization proposed by Sitch et al. (2007) to account for ozone damage to photosynthesis through stomatal uptake. The scheme simulates associated changes in both photosynthetic rate and stomatal conductance.

GMDD
8, 3147–3196, 2015

When photosynthesis is inhibited by ozone, stomatal conductance decreases accordingly to resist more ozone molecules. We employed an off-line regional version of YIBs to show that present-day ozone damage decreases GPP by 4–8 % on average in the eastern US and leads to larger decreases of 11–17 % in east coast hotspots (Yue and Unger, 2014). In the current model version, the photosynthesis and stomatal conductance responses to ozone damage are coupled. In future work, we will update the ozone vegetation damage function in YIBs to account for decoupled photosynthesis and stomatal conductance responses based on recent extensive meta-data analyses (Wittig et al., 2007; Lombardozzi et al., 2013).

3.6 Biogenic volatile organic compound (BVOC) emissions

YIBs incorporates two independent leaf-level isoprene emission schemes embedded within the exact same host model framework (Zheng et al., 2015). The photosynthesis-based isoprene scheme simulates emission as a function of the electron transport-limited photosynthesis rate (J_e, Eq. 3), canopy temperature, intercellular CO_2 (c_i) and Γ_* (Arneth et al., 2007; Unger et al., 2013). The MEGAN scheme applies the commonly used leaf-level functions of light and canopy temperature (Guenther et al., 1993, 1995, 2012). Both isoprene schemes account for atmospheric CO_2-sensitivity (Arneth et al., 2007). Long-term increases (decreases) in atmospheric CO_2 decrease (increase) isoprene emissions (Unger et al., 2013). The CO_2-sensitivity is higher under lower vs. higher atmospheric CO_2 levels than present day. Leaf-level monoterpene emissions are simulated using a simplified temperature dependent algorithm (Lathiere et al., 2006). The leaf-level isoprene and monoterpene emissions are integrated over the multiple canopy layers in the exact same way as GPP to obtain the total canopy-level emissions.

GMDD
8, 3147–3196, 2015

3.7 Implementation of YIBs into NASA ModelE2 (NASA ModelE2-YIBs)

NASA ModelE2 has a spatial resolution of $2^{\circ} \times 2.5^{\circ}$ latitude by longitude with 40 vertical levels extending to 0.1 hPa. In the on-line configuration, the global climate model provides the meteorological drivers to YIBs and the land-surface hydrology submodel provides the soil characteristics (Rosenzweig and Abramopoulos, 1997; Schmidt et al., 2014). Recent relevant updates to NASA ModelE2 include a dynamic fire activity parameterization from Pechony and Shindell (2009) and climate-sensitive soil NO_x emissions based on Yienger and Levy (1995) (Unger and Yue, 2014). Without the YIBs implementation, the default NASA ModelE2 computes dry deposition using fixed LAI and vegetation cover fields from Olson et al. (2001), which are different from the climate model's vegetation scheme. With YIBs embedded in NASA ModelE2, the YIBs model provides the vegetation cover and LAI for the dry deposition scheme. The on-line simulated atmospheric ozone and aerosol concentrations influence terrestrial carbon assimilation and stomatal conductance at the 30 min integration time step. In turn, the on-line vegetation properties, and water, energy and BVOC fluxes affect air quality, meteorology and the atmospheric chemical composition. The model simulates the deposition of inorganic and organic nitrogen to the terrestrial biosphere. However, the YIBs biosphere currently applies fixed nitrogen levels and does not yet account for the dynamic interactions between the carbon and nitrogen cycles, and the consequences for carbon assimilation, which are highly uncertain (e.g., Thornton et al., 2007).

4 Model setup and simulations

4.1 Site-level simulations (YIBs-site)

We perform site-level simulations with offline YIBs model at 145 eddy covariance flux tower sites for the corresponding PFTs (Fig. 1). Hourly in situ measurements of meteorology (Sect. 2.1) are used as input for the model. We gap filled missing measurements

GMDD
8, 3147–3196, 2015

with the Global Modeling and Assimilation Office (GMAO) Modern Era-Retrospective Analysis (MERRA) reanalysis (Rienecker et al., 2011), as described in Yue and Unger (2014). All grasslands and most croplands are considered as C_3 plants, except for some sites where corn is grown. Meteorological measurements are available for a wide range of time periods across the different sites ranging from the minimum of 1 year at some sites (e.g. BE-Jal) and the maximum of 16 years at Harvard Forest (US-HA1). For each site, we spin up the YIBs model for 30 years with the initial height H_0 for corresponding PFT (Table 1) and the fixed meteorology and CO_2 concentrations at the first year of observations, and then continue simulations with year-to-year observations at the same site for the rest of observation period. For all grass and shrub sites, two simulations are performed. One applies additional drought controls on phenology as described in Sects. 3.2.2 and 3.2.3, while the other uses only temperature-dependent phenology. By comparing results of these two simulations, we assess the role of drought phenology for plants in arid and semi-arid regions.

4.2 Global off-line simulation (YIBs-offline)

The global off-line YIBs applies the CLM land cover dataset (Oleson et al., 2010). Land cover is derived based on retrievals from both MODIS (Hansen et al., 2003) and AVHRR (Defries et al., 2000). Fractions of 16 PFTs are aggregated into 9 model PFTs (Table 1). The global off-line YIBs model is driven with WFDEI meteorology (Weedon et al., 2014) at $1^\circ \times 1^\circ$ horizontal resolution for the period of 1980–2011. Tree height and soil carbon pools from the spin-up process (Supplement) are used as initial conditions. Observed atmospheric CO_2 concentrations are adopted from the fifth assessment report (AR5) of the Intergovernmental Panel on Climate Change (IPCC) (Meinshausen et al., 2011). We evaluate the simulated long-term average tree height/LAI and carbon fluxes with available observations and recent multi-model inter-comparisons. Attribution of the decadal trends in terrestrial carbon fluxes are explored in a separate follow-on companion study (Yue et al., 2015b).

GMDD
8, 3147–3196, 2015

4.3 Global on-line simulation in NASA ModelE2-YIBs

The global land cover data is identical to that used in YIBs-offline (Sect. 4.2) based on the CLM cover. Because our major research goal is to study short-term (seasonal, annual, decadal) interactions between vegetation physiology and atmospheric chemistry, we elect to prescribe the PFT distribution in different climatic states. We perform an on-line atmosphere-only simulation representative of the present day (~ 2000s) climatology by prescribing fixed monthly-average sea surface temperature (SST) and sea ice temperature for the 1996–2005 decade from the Hadley Center as the boundary conditions (Rayner et al., 2006). Atmospheric CO_2 concentration is fixed at the level of the year 2000 (370 ppm). The spin-up process described in Supplement using the off-line YIBs model is repeated but with fixed WFDEI meteorology and [CO_2] at the year 2000 values. We use the derived tree height and soil pools as initial conditions for the on-line NASA ModelE2-YIBs present-day simulation and run for 30 model years. The first 20 years are discarded as the on-line spin-up and the last 10 year results are averaged for the analyses including comparisons with observations and the YIBs-offline.

4.4 Ozone vegetation damage simulation (YIBs-ozone)

We perform two simulations to quantify ozone vegetation damage with the off-line YIBs model based on the high and low ozone sensitivity parameterizations (Sitch et al., 2007). Similar to the set up in Yue and Unger (2014), we use off-line hourly surface ozone concentrations simulated with the NASA ModelE2 based on the climatology and precursor emissions of the year 2000 (Sect. 4.3). In this way, atmospheric ozone photosynthesis damage affects plant growth, including changes in tree height and LAI. We compare the simulated ozone damage effects with the previous results in Yue and Unger (2014) that used prescribed LAI. For this updated assessment, we do not isolate possible feedbacks from the resultant land carbon cycle changes to the surface ozone concentrations themselves, for instance through concomitant changes to BVOC emis-

GMDD
8, 3147–3196, 2015

sions and water fluxes. The importance of these feedbacks will be quantified in future research using the on-line NASA ModelE2-YIBs framework.

5 Results

5.1 Site-level evaluation

The simulated monthly-average GPP is compared with measurements at 145 sites for different PFTs (Fig. 3). GPP simulation biases range from −19 to 7 % depending on PFT. The highest correlation of 0.86 is achieved for DBF, mainly contributed by the reasonable phenology simulated at these sites (Fig. S2). The correlation is also high for ENF sites, because the inhibition of V_{cmax} by frost hardening captures the observed low GPP in cold seasons even though phenology is set to a constant value of 1.0. A relatively low correlation of 0.65 is modeled for EBF sites (Fig. S2). However, the site-specific evaluation shows that the simulations reasonably capture the observed magnitude and seasonality, including the minimum GPP in summer due to drought at some sites (e.g. FR-Pue and IT-Lec). Predictions at crop sites achieve a medium correlation of 0.77, because the prescribed crop phenology based on the planting and harvesting dates dataset matches reality for most sites with some exceptions (e.g. CH-Oe2). Measured GPP at shrub and grass sites show varied seasonality. For most sites, the maximum carbon fluxes are measured in the hemispheric summer season. However, for sites with arid or Mediterranean climate, the summer GPP is usually the lowest during the year (e.g. ES-LMa and US-Var in Fig. S2) while the peak flux is observed during the wet season when the climate is cooler and moister. Implementing the drought-dependent phenology helps improve the GPP seasonality and decrease the root-mean-square error (RMSE) at most warm climate shrub and grass sites (Fig. S3).

A synthesis of the site-level evaluation is presented in Fig. 4. Among the 145 sites, 121 have correlations higher than 0.8 for the GPP simulation (Fig. 4a). Predictions are better for PFTs with larger seasonal variations. For example, high correlations of

GMDD
8, 3147–3196, 2015

> 0.8 are achieved at 95 % ENF and DBF sites, but only 70 % for grass and 45 % for EBF sites. Low relative biases (−33 to 50 %) are achieved at 94 sites (Fig. 4c). For most PFTs, a similar fraction (65 %) of the sites have low biases falling into that range, except for cropland, where only 7 sites (45 %) have the low biases. The RMSE is lower than 3 g[C] day^{-1} for 107 out of 145 sites (Fig. 4e). The highest RMSE is predicted for crop sites, where the model misses the large interannual variations due to crop rotation at some sites (e.g. BE-Lon, DE-Geb, and US-Ne2).

Compared with GPP, the NEE simulations have smaller correlations with measurements because of the limited seasonality in the observations at most sites (Fig. S4). 74 sites (51 %) have correlation coefficients higher than 0.6 (Fig. 4b) and 75 sites (52 %) have absolute biases within ±0.5 g[C] day^{-1} (Fig. 4d). For most ENF sites, the maximum net carbon uptake (the minimum NEE) is observed in spring or early summer, when GPP begins to increase while soil respiration is still at low rate due to the cool and wet conditions (e.g. CA-Ojp and ES-ES1). Compared with other PFTs, the DBF trees usually have larger seasonality with the NEE peak in the early summer. Such seasonality helps promote correlations between model and measurements, resulting in high R (> 0.8) for 17 out of 20 sites (Fig. 4b). For shrub and grass sites, the observed seasonality of NEE is not regular, though most show maximum carbon uptake in spring or early summer. Implementation of drought-dependent phenology helps improve the simulated NEE seasonality at some sites of these PFTs (e.g. ES-LMa and IT-Pia), however, such improvement is limited for others (Fig. S4). Simulated crop NEE reaches maximum magnitude in summer at most sites, consistent with observations and leading to a high R (> 0.8) for 10 out 16 sites (Fig. 4b). The RMSE of simulated NEE is larger for crop relative to other PFTs because the model does not treat crop rotation (Fig. 4f).

5.2 Evaluation of YIBs-offline

YIBs-offline forced with WFDEI meteorology simulates reasonable spatial distributions for tree height, LAI, and GPP, all of which show maximums in the tropical rainforest

GMDD
8, 3147–3196, 2015

biome and medium values in the Northern Hemisphere high latitudes (Fig. 5). Compared with the satellite observations, the simulated height is underestimated by 30 % on the annual and global mean basis (Fig. 5b). Regionally, the prediction is larger by only 4 % for tropical rainforest and temperate DBF, but by 27 % for boreal ENF, for which the model assumes a constant phenology of 1.0 all the year round. However, for the vast areas covered with grass and shrub PFTs, the simulated height is lower by 41 % with maximum underestimation in Eastern Siberia, where the model land is covered by short tundra. The modeled LAI is remarkably close to observations on the annual and global mean basis (Fig. 5c and d). However, there are substantial regional biases in model LAI. Model LAI prediction is higher by 0.8 $m^2 m^{-2}$ (70 %) for boreal ENF and by 0.1 $m^2 m^{-2}$ (5 %) for tropical rainforest. In contrast, the simulation underestimates LAI of tropical C_4 grass by 0.4 $m^2 m^{-2}$ (30 %) and shrubland by 0.2 $m^2 m^{-2}$ (30 %). The GPP simulation is lower than the FLUXNET-derived value by 5 % on the global scale, which is contributed by the minor underestimation for all PFTs except for tropical rainforest, where model predicts 9 % higher GPP than observations (Fig. 5f).

The model simulates reasonable seasonality for LAI and land carbon fluxes (Fig. 6). Tree height shows limited seasonal variations, especially for DBF, ENF, and EBF trees. LAI, GPP, and NPP also exhibit small seasonality over tropical areas, such as the Amazon, Central Africa, and Indonesia. However, for temperate areas, such as North America, Europe and East Asia, these variables show large seasonal variations with minimum in winter and maximum in summer. The LAI is overestimated by 20 % in Amazon during the December-January-February season but underestimated by 25 % in Indonesia during summer (Fig. 6b). For GPP and NPP, the positive bias in Indonesia is even larger at 45 % during summer (Fig. 6c and d).

On the global scale, YIBs-offline simulates GPP of $124.6 \pm 3.3\,Pg\,C\,a^{-1}$ and NEE of $-2.5 \pm 0.7\,Pg\,C\,a^{-1}$ for 1982–2011. These values are consistent with estimates upscaled from the FLUXNET observations (Jung et al., 2009; Friedlingstein et al., 2010; Jung et al., 2011) and simulations from 10 other carbon cycle models (Piao et al., 2013) (Fig. 7). The net biome productivity (NBP) is in opposite sign to NEE. Tropi-

GMDD
8, 3147–3196, 2015

cal areas account for 53 % of the global GPP, including 27 % from Amazon rainforest, 21 % from central Africa, and 5 % from Indonesia forest (Table 3). A lower contribution of 46 % from tropics is predicted for NPP and heterotrophic respiration. However, for NEE, only 32 % of the land carbon sink is contributed by tropical forests and grasslands, while 56 % is from temperate forests and grasslands in North America, Europe, and East Asia. The NEE differences between the tropical and temperate biomes are largely driven by the higher dark respiration rate and enhanced autotrophic respiration in the warmer climate zone.

We compare the simulated budburst dates with observations from satellite retrieval (Fig. 8). The model captures the basic spatial pattern of spring phenology with earlier to later budburst dates from lower to higher latitudes. On average, the observed budburst date in Northern Hemisphere (NH) is 133 DOY (13 May) and simulation is 132 DOY (12 May). Such close estimate results from the regional delay of 10 days (119 vs. 129 DOY) in Europe and advance of 4 days (140 vs. 136 DOY) in East Asia. In Y2015, extensive (~ 75 000 records) ground-based measurements have been used to validate the simulated spring and autumn phenology in US and both the spatial distribution and interannual variation of simulation are reasonable.

5.3 Evaluation of NASA ModelE2-YIBs

NASA ModelE2-YIBs simulations of global land carbon fluxes show similar spatial distribution and magnitude as the YIBs-offline model (Figs. S6–S8). However, due to differences in the meteorological forcings (Figs. S9–S12), regional discrepancies between the two configurations occur. The predicted LAI with NASA ModelE2-YIBs is lower by 20 % in Amazon region than YIBs-offline (Fig. S6), following the similar magnitude of differences in regional GPP and NPP (Figs. S7 and S8). We performed driver attribution sensitivity simulations, in which the YIBs-offline configuration is driven with the same meteorological forcings simulated by NASA ModelE2 except for one selected field from the WFDEI reanalysis. We found that the anomalously warmer climate over the Amazon in the global climate model (Fig. S9) causes the lower GPP in that region

GMDD
8, 3147–3196, 2015

in NASA ModelE2-YIBs. The temperature optimum for C_3 photosynthesis is around 30 °C, above which the maximum rate of electron transport (Eq. 3) decreases dramatically (Farquhar et al., 1980). As a result, the higher NASA ModelE2-YIBs surface temperature in the tropical rainforest results in the lower photosynthesis rates there. With the exception of the Amazon, the NASA ModelE2-YIBs June-July-August GPP and NPP show low biases in central Africa and high latitudes in North America and Asia, but high biases in Europe, western US, and eastern China (Figs. S7 and S8). The sensitivity tests attribute these discrepancies to differences in canopy humidity (Fig. S11) and soil wetness (Fig. S12). Low soil wetness decreases water stress β, reduces the slope m of Ball–Berry equation (Eq. 6), and consequently limits photosynthesis by declining stomatal conductance in combination with low humidity. On the global scale, the ModelE2-YIBs simulates annual GPP of 122.9 Pg C, NPP of 62 Pg C, and NEE of −2.7 Pg C, all of which are close to the YIBs-offline simulation (Table 3) and consistent with results from observations and model inter-comparison (Fig. 7).

5.4 Assessment of global ozone vegetation damage

Ozone dampens GPP and consequently affects tree growth and LAI. In North America, the annual average reductions range from 2 to 6 %, depending on the plant sensitivity to ozone damage (Table 3). Locally, average damages reach as high as 5–11 % in the eastern US with maximums up to 11–23 % (Fig. 9a and b). These values are higher than the estimate of 4–8 % (maximum 11–17 %) by Yue and Unger (2014), because the latter used prescribed LAI in the simulation and did not consider the LAI reductions due to ozone damage (Fig. 9c and d). The YIBs model predicts similar magnitude of damages in Europe compared to North America, but almost doubled effects in East Asia (Table 3) due to the high ozone concentrations there, especially in boreal summer (Fig. S5). Ozone-induced GPP-reductions are limited in tropical areas (Fig. 5e) because the surface ozone levels there are very low, for example, especially over the Amazon forest (Fig. S5). The damage to LAI generally follows the pattern of GPP reductions but the response signal is weaker than that of GPP (Fig. 9c and d).

GMDD
8, 3147–3196, 2015

6 Conclusions and discussion

We describe and evaluate the process-based YIBs interactive terrestrial biosphere model. YIBs is embedded into the NASA ModelE2 global chemistry–climate model and is an important urgently needed development to improve the biological realism of interactions between vegetation, atmospheric chemistry and climate. We implement both temperature- and drought-dependent phenology for DBF, shrub, and grass species. The model simulates interactive ozone vegetation damage. The YIBs model is fully validated with land carbon flux measurements from 145 ground stations and global observations of canopy height, LAI, GPP, NPP, and phenology from multiple satellite retrievals.

There are several limitations in the current model set up. The vegetation parameters, V_{cmax25}, m, and b (Table 1), are not well calibrated for the tropical rainforest biome due to the limited availability of tropical site measurement data (Fig. 1). The model does not yet include a dynamic treatment of nitrogen and phosphorous availability (Thornton et al., 2007; Zaehle et al., 2014). Phenology is set to a constant value of 1 for ENF and EBF, which is not consistent with observations (O'Keefe, 2000; Jones et al., 2014). The ozone damage scheme of Sitch et al. (2007) considers coupled responses of photosynthesis and stomatal conductance while observations suggest a decoupling (Lombardozzi et al., 2013).

Despite these limitations, the YIBs model reasonably simulates global land carbon fluxes compared with both site-level flux measurements and global satellite observations. YIBs is primed for on-going development, for example, incorporating community dynamics including mortality, establishment, seed transport and dynamic fire disturbance (Moorcroft et al., 2001). NASA ModelE2-YIBs is available to be integrated with interactive ocean and atmospheric carbon components to offer a full global carbon-climate model, for example for use in interpreting and diagnosing new satellite datasets of atmospheric CO_2 concentrations. In the current form, NASA ModelE2-YIBs provides a useful new tool to investigate the impacts of air pollution on the carbon budget, water

GMDD
8, 3147–3196, 2015

cycle, and surface energy balance, and, in turn, the impacts of changing vegetation physiology on the atmospheric chemical composition. Carbon–chemistry–climate interactions, a relatively new interdisciplinary research frontier, are expected to influence the evolution of the Earth's climate system on multiple spatiotemporal scales.

The Supplement related to this article is available online at doi:10.5194/gmdd-8-3147-2015-supplement.

Acknowledgements. Funding support for this research is provided by the NASA Atmospheric Composition Campaign Data Analysis and Modeling Program. This project was supported in part by the facilities and staff of the Yale University Faculty of Arts and Sciences High Performance Computing Center. The authors would like to thank Ranga B. Myneni and Zaichun Zhu for providing the AVHRR LAI3g dataset.

References

Ainsworth, E. A., Yendrek, C. R., Sitch, S., Collins, W. J., and Emberson, L. D.: The effects of tropospheric ozone on net primary productivity and implications for climate change, Annu. Rev. Plant Biol., 63, 637–661, 2012.

Arneth, A., Niinemets, Ü., Pressley, S., Bäck, J., Hari, P., Karl, T., Noe, S., Prentice, I. C., Serça, D., Hickler, T., Wolf, A., and Smith, B.: Process-based estimates of terrestrial ecosystem isoprene emissions: incorporating the effects of a direct CO_2-isoprene interaction, Atmos. Chem. Phys., 7, 31–53, doi:10.5194/acp-7-31-2007, 2007.

Baldocchi, D.: An analytical solution for coupled leaf photosynthesis and stomatal conductance models, Tree Physiol., 14, 1069–1079, 1994.

Beer, C., Reichstein, M., Tomelleri, E., Ciais, P., Jung, M., Carvalhais, N., Rodenbeck, C., Arain, M. A., Baldocchi, D., Bonan, G. B., Bondeau, A., Cescatti, A., Lasslop, G., Lindroth, A., Lomas, M., Luyssaert, S., Margolis, H., Oleson, K. W., Roupsard, O., Veenendaal, E., Viovy, N., Williams, C., Woodward, F. I., and Papale, D.: Terrestrial gross car-

GMDD
8, 3147–3196, 2015

bon dioxide uptake: global distribution and covariation with climate, Science, 329, 834–838, doi:10.1126/Science.1184984, 2010.

Bonan, G. B., Levis, S., Sitch, S., Vertenstein, M., and Oleson, K. W.: A dynamic global vegetation model for use with climate models: concepts and description of simulated vegetation dynamics, Global Change Biol., 9, 1543–1566, doi:10.1046/J.1365-2486.2003.00681.X, 2003.

Bonan, G. B., Lawrence, P. J., Oleson, K. W., Levis, S., Jung, M., Reichstein, M., Lawrence, D. M., and Swenson, S. C.: Improving canopy processes in the Community Land Model version 4 (CLM4) using global flux fields empirically inferred from FLUXNET data, J. Geophys. Res., 116, G02014, doi:10.1029/2010jg001593, 2011.

Clark, D. B., Mercado, L. M., Sitch, S., Jones, C. D., Gedney, N., Best, M. J., Pryor, M., Rooney, G. G., Essery, R. L. H., Blyth, E., Boucher, O., Harding, R. J., Huntingford, C., and Cox, P. M.: The Joint UK Land Environment Simulator (JULES), model description – Part 2: Carbon fluxes and vegetation dynamics, Geosci. Model Dev., 4, 701–722, doi:10.5194/gmd-4-701-2011, 2011.

Collatz, G. J., Ball, J. T., Grivet, C., and Berry, J. A.: Physiological and environmental-regulation of stomatal conductance, photosynthesis and transpiration – a model that includes a laminar boundary-layer, Agr. Forest Meteorol., 54, 107–136, doi:10.1016/0168-1923(91)90002-8, 1991.

Cox, P. M.: Description of the "TRIFFID" Dynamic Global Vegetation Model, Hadley Centre technical note 24, 2001.

Defries, R. S., Hansen, M. C., Townshend, J. R. G., Janetos, A. C., and Loveland, T. R.: A new global 1-km dataset of percentage tree cover derived from remote sensing, Global Change Biol., 6, 247–254, doi:10.1046/J.1365-2486.2000.00296.X, 2000.

Delbart, N. and Picard, G.: Modeling the date of leaf appearance in low-arctic tundra, Global Change Biol., 13, 2551–2562, doi:10.1111/J.1365-2486.2007.01466.X, 2007.

Delpierre, N., Dufrene, E., Soudani, K., Ulrich, E., Cecchini, S., Boe, J., and Francois, C.: Modelling interannual and spatial variability of leaf senescence for three deciduous tree species in France, Agr. Forest Meteorol., 149, 938–948, doi:10.1016/J.Agrformet.2008.11.014, 2009.

Doughty, C. E. and Goulden, M. L.: Seasonal patterns of tropical forest leaf area index and CO_2 exchange, J. Geophys. Res., 113, G00b06, doi:10.1029/2007jg000590, 2008.

GMDD
8, 3147–3196, 2015

Dufrene, E., Davi, H., Francois, C., le Maire, G., Le Dantec, V., and Granier, A.: Modelling carbon and water cycles in a beech forest Part I: Model description and uncertainty analysis on modelled NEE, Ecol. Model., 185, 407–436, doi:10.1016/J.Ecolmodel.2005.01.004, 2005.

Farquhar, G. D., Caemmerer, S. V., and Berry, J. A.: A biochemical-model of photosynthetic CO_2 assimilation in leaves of C_3 Species, Planta, 149, 78–90, doi:10.1007/Bf00386231, 1980.

Friedlingstein, P., Cox, P., Betts, R., Bopp, L., Von Bloh, W., Brovkin, V., Cadule, P., Doney, S., Eby, M., Fung, I., Bala, G., John, J., Jones, C., Joos, F., Kato, T., Kawamiya, M., Knorr, W., Lindsay, K., Matthews, H. D., Raddatz, T., Rayner, P., Reick, C., Roeckner, E., Schnitzler, K. G., Schnur, R., Strassmann, K., Weaver, A. J., Yoshikawa, C., and Zeng, N.: Climate–carbon cycle feedback analysis: results from the (CMIP)-M-4 model intercomparison, J. Climate, 19, 3337–3353, doi:10.1175/Jcli3800.1, 2006.

Friedlingstein, P., Houghton, R. A., Marland, G., Hackler, J., Boden, T. A., Conway, T. J., Canadell, J. G., Raupach, M. R., Ciais, P., and Le Quere, C.: Update on CO_2 emissions, Nat. Geosci., 3, 811–812, doi:10.1038/Ngeo1022, 2010.

Friedlingstein, P., Andrew, R. M., Rogelj, J., Peters, G. P., Canadell, J. G., Knutti, R., Luderer, G., Raupach, M. R., Schaeffer, M., van Vuuren, D. P., and Le Quere, C.: Persistent growth of CO_2 emissions and implications for reaching climate targets, Nat. Geosci., 7, 709–715, doi:10.1038/Ngeo2248, 2014.

Friend, A. D. and Kiang, N. Y.: Land surface model development for the GISS GCM: effects of improved canopy physiology on simulated climate, J. Climate, 18, 2883–2902, doi:10.1175/Jcli3425.1, 2005.

Gill, R. A. and Jackson, R. B.: Global patterns of root turnover for terrestrial ecosystems, New Phytol., 147, 13–31, doi:10.1046/J.1469-8137.2000.00681.X, 2000.

Guenther, A. B., Hewitt, C. N., Erickson, D., Fall, R., Geron, C., Graedel, T., Harley, P., Klinger, L., Lerdau, M., Mckay, W. A., Pierce, T., Scholes, B., Steinbrecher, R., Tallamraju, R., Taylor, J., and Zimmerman, P.: A global-model of natural volatile organic-compound emissions, J. Geophys. Res., 100, 8873–8892, doi:10.1029/94jd02950, 1995.

Guenther, A. B., Zimmerman, P. R., Harley, P. C., Monson, R. K., and Fall, R.: Isoprene and monoterpene emission rate variability – model evaluations and sensitivity analyses, J. Geophys. Res., 98, 12609–12617, doi:10.1029/93jd00527, 1993.

Guenther, A. B., Jiang, X., Heald, C. L., Sakulyanontvittaya, T., Duhl, T., Emmons, L. K., and Wang, X.: The Model of Emissions of Gases and Aerosols from Nature version 2.1

GMDD
8, 3147–3196, 2015

(MEGAN2.1): an extended and updated framework for modeling biogenic emissions, Geosci. Model Dev., 5, 1471–1492, doi:10.5194/gmd-5-1471-2012, 2012.
Hanninen, H. and Kramer, K.: A framework for modelling the annual cycle of trees in boreal and temperate regions, Silva Fenn., 41, 167–205, 2007.
Hansen, M. C., DeFries, R. S., Townshend, J. R. G., Carroll, M., Dimiceli, C., and Sohlberg, R. A.: Global percent tree cover at a spatial resolution of 500 meters: first results of the MODIS vegetation continuous fields algorithm, Earth Interact., 7, 1–15, doi:10.1175/1087-3562(2003)007<0001:GPTCAA>2.0.CO;2, 2003.
Hollaway, M. J., Arnold, S. R., Challinor, A. J., and Emberson, L. D.: Intercontinental trans-boundary contributions to ozone-induced crop yield losses in the Northern Hemisphere, Biogeosciences, 9, 271–292, doi:10.5194/bg-9-271-2012, 2012.
Houghton, R. A., House, J. I., Pongratz, J., van der Werf, G. R., DeFries, R. S., Hansen, M. C., Le Quéré, C., and Ramankutty, N.: Carbon emissions from land use and land-cover change, Biogeosciences, 9, 5125–5142, doi:10.5194/bg-9-5125-2012, 2012.
Huntingford, C., Cox, P. M., Mercado, L. M., Sitch, S., Bellouin, N., Boucher, O., and Gedney, N.: Highly contrasting effects of different climate forcing agents on terrestrial ecosystem services, Philos. T. R. Soc. A, 369, 2026–2037, doi:10.1098/Rsta.2010.0314, 2011.
Jones, M. O., Kimball, J. S., and Nemani, R. R.: Asynchronous Amazon forest canopy phenology indicates adaptation to both water and light availability, Environ. Res. Lett., 9, 124021, doi:10.1088/1748-9326/9/12/124021, 2014.
Jung, M., Reichstein, M., and Bondeau, A.: Towards global empirical upscaling of FLUXNET eddy covariance observations: validation of a model tree ensemble approach using a biosphere model, Biogeosciences, 6, 2001–2013, doi:10.5194/bg-6-2001-2009, 2009.
Jung, M., Reichstein, M., Margolis, H. A., Cescatti, A., Richardson, A. D., Arain, M. A., Arneth, A., Bernhofer, C., Bonal, D., Chen, J. Q., Gianelle, D., Gobron, N., Kiely, G., Kutsch, W., Lasslop, G., Law, B. E., Lindroth, A., Merbold, L., Montagnani, L., Moors, E. J., Papale, D., Sottocornola, M., Vaccari, F., and Williams, C.: Global patterns of land–atmosphere fluxes of carbon dioxide, latent heat, and sensible heat derived from eddy covariance, satellite, and meteorological observations, J. Geophys. Res., 116, G00j07, doi:10.1029/2010jg001566, 2011.
Keenan, T. F., Gray, J., Friedl, M. A., Toomey, M., Bohrer, G., Hollinger, D. Y., Munger, J. W., O'Keefe, J., Schmid, H. P., SueWing, I., Yang, B., and Richardson, A. D.: Net carbon uptake

GMDD
8, 3147–3196, 2015

has increased through warming-induced changes in temperate forest phenology, Nat. Clim. Change, 4, 598–604, doi:10.1038/Nclimate2253, 2014.
Kim, Y. and Wang, G. L.: Modeling seasonal vegetation variation and its validation against Moderate Resolution Imaging spectroradiometer (MODIS) observations over North America, J. Geophys. Res., 110, D04106, doi:10.1029/2004jd005436, 2005.
Knorr, W.: Annual and interannual CO_2 exchanges of the terrestrial biosphere: process-based simulations and uncertainties, Global Ecol. Biogeogr., 9, 225–252, doi:10.1046/J.1365-2699.2000.00159.X, 2000.
Koch, D., Bauer, S. E., Del Genio, A., Faluvegi, G., McConnell, J. R., Menon, S., Miller, R. L., Rind, D., Ruedy, R., Schmidt, G. A., and Shindell, D.: Coupled aerosol–chemistry–climate twentieth-century transient model investigation: trends in short-lived species and climate responses, J. Climate, 24, 2693–2714, doi:10.1175/2011jcli3582.1, 2011.
Lathière, J., Hauglustaine, D. A., Friend, A. D., De Noblet-Ducoudré, N., Viovy, N., and Folberth, G. A.: Impact of climate variability and land use changes on global biogenic volatile organic compound emissions, Atmos. Chem. Phys., 6, 2129–2146, doi:10.5194/acp-6-2129-2006, 2006.
Liu, H., Tian, F., Hu, H. C., Hu, H. P., and Sivapalan, M.: Soil moisture controls on patterns of grass green-up in Inner Mongolia: an index based approach, Hydrol. Earth Syst. Sci., 17, 805–815, doi:10.5194/hess-17-805-2013, 2013.
Lombardozzi, D., Sparks, J. P., and Bonan, G.: Integrating O_3 influences on terrestrial processes: photosynthetic and stomatal response data available for regional and global modeling, Biogeosciences, 10, 6815–6831, doi:10.5194/bg-10-6815-2013, 2013.
Mahowald, N.: Aerosol indirect effect on biogeochemical cycles and climate, Science, 334, 794–796, doi:10.1126/Science.1207374, 2011.
Meinshausen, M., Smith, S. J., Calvin, K., Daniel, J. S., Kainuma, M. L. T., Lamarque, J. F., Matsumoto, K., Montzka, S. A., Raper, S. C. B., Riahi, K., Thomson, A., Velders, G. J. M., and van Vuuren, D. P. P.: The RCP greenhouse gas concentrations and their extensions from 1765 to 2300, Climatic Change, 109, 213–241, doi:10.1007/S10584-011-0156-Z, 2011.
Mercado, L. M., Bellouin, N., Sitch, S., Boucher, O., Huntingford, C., Wild, M., and Cox, P. M.: Impact of changes in diffuse radiation on the global land carbon sink, Nature, 458, 1014–1087, doi:10.1038/Nature07949, 2009.
Miller, R. L., Schmidt, G. A., Nazarenko, L. S., Tausnev, N., Bauer, S. E., DelGenio, A. D., Kelley, M., Lo, K. K., Ruedy, R., Shindell, D. T., Aleinov, I., Bauer, M., Bleck, R., Canuto, V.,

GMDD
8, 3147–3196, 2015

Chen, Y. H., Cheng, Y., Clune, T. L., Faluvegi, G., Hansen, J. E., Healy, R. J., Kiang, N. Y., Koch, D., Lacis, A. A., LeGrande, A. N., Lerner, J., Menon, S., Oinas, V., Garcia-Pando, C. P., Perlwitz, J. P., Puma, M. J., Rind, D., Romanou, A., Russell, G. L., Sato, M., Sun, S., Tsigaridis, K., Unger, N., Voulgarakis, A., Yao, M. S., and Zhang, J. L.: CMIP5 historical simulations (1850–2012) with GISS ModelE2, J. Adv. Model. Earth Syst., 6, 441–477, doi:10.1002/2013ms000266, 2014.

Moorcroft, P. R., Hurtt, G. C., and Pacala, S. W.: A method for scaling vegetation dynamics: the ecosystem demography model (ED), Ecol. Monogr., 71, 557–585, doi:10.1890/0012-9615(2001)071[0557:Amfsvd]2.0.Co;2, 2001.

Murray, M. B., Cannell, M. G. R., and Smith, R. I.: Date of budburst of fifteen tree species in Britain following climatic warming, J. Appl. Ecol., 26, 693–700, doi:10.2307/2404093, 1989.

O'Keefe, J.: Phenology of Woody Species at Harvard Forest since 1990, Harvard Forest Data Archive: HF003, 2000.

Oleson, K. W., Lawrence, D. M., Bonan, G. B., Flanne, M. G., Kluzek, E., Lawrence, P. J., Levis, S., Swenson, S. C., and Thornton, P. E.: Technical Description of version 4.0 of the Community Land Model (CLM), National Center for Atmospheric Research, Boulder, CONCAR/TN-478+STR, 2010.

Olson, D. M., Dinerstein, E., Wikramanayake, E. D., Burgess, N. D., Powell, G. V. N., Underwood, E. C., D'amico, J. A., Itoua, I., Strand, H. E., Morrison, J. C., Loucks, C. J., Allnutt, T. F., Ricketts, T. H., Kura, Y., Lamoreux, J. F., Wettengel, W. W., Hedao, P., and Kassem, K. R.: Terrestrial ecoregions of the world: a new map of life on earth, Bioscience, 51, 933–938, doi:10.1641/0006-3568(2001)051[0933:TEOTWA]2.0.CO;2, 2001.

Pechony, O. and Shindell, D. T.: Fire parameterization on a global scale, J. Geophys. Res., 114, D16115, doi:10.1029/2009jd011927, 2009.

Piao, S. L., Sitch, S., Ciais, P., Friedlingstein, P., Peylin, P., Wang, X. H., Ahlstrom, A., Anav, A., Canadell, J. G., Cong, N., Huntingford, C., Jung, M., Levis, S., Levy, P. E., Li, J. S., Lin, X., Lomas, M. R., Lu, M., Luo, Y. Q., Ma, Y. C., Myneni, R. B., Poulter, B., Sun, Z. Z., Wang, T., Viovy, N., Zaehle, S., and Zeng, N.: Evaluation of terrestrial carbon cycle models for their response to climate variability and to CO_2 trends, Global Change Biol., 19, 2117–2132, doi:10.1111/Gcb.12187, 2013.

Porporato, A., Laio, F., Ridolfi, L., and Rodriguez-Iturbe, I.: Plants in water-controlled ecosystems: active role in hydrologic processes and response to water stress – III. Vegetation water stress, Adv. Water Resour., 24, 725–744, doi:10.1016/S0309-1708(01)00006-9, 2001.

GMDD
8, 3147–3196, 2015

Rayner, N. A., Brohan, P., Parker, D. E., Folland, C. K., Kennedy, J. J., Vanicek, M., Ansell, T. J., and Tett, S. F. B.: Improved analyses of changes and uncertainties in sea surface temperature measured in situ sice the mid-nineteenth century: the HadSST2 dataset, J. Climate, 19, 446–469, doi:10.1175/Jcli3637.1, 2006.

Richardson, A. D., Bailey, A. S., Denny, E. G., Martin, C. W., and O'Keefe, J.: Phenology of a northern hardwood forest canopy, Global Change Biol., 12, 1174–1188, doi:10.1111/j.1365-2486.2006.01164.x, 2006.

Richardson, A. D., Keenan, T. F., Migliavacca, M., Ryu, Y., Sonnentag, O., and Toomey, M.: Climate change, phenology, and phenological control of vegetation feedbacks to the climate system, Agr. Forest Meteorol., 169, 156–173, 2013.

Rienecker, M. M., Suarez, M. J., Gelaro, R., Todling, R., Bacmeister, J., Liu, E., Bosilovich, M. G., Schubert, S. D., Takacs, L., Kim, G. K., Bloom, S., Chen, J. Y., Collins, D., Conaty, A., Da Silva, A., Gu, W., Joiner, J., Koster, R. D., Lucchesi, R., Molod, A., Owens, T., Pawson, S., Pegion, P., Redder, C. R., Reichle, R., Robertson, F. R., Ruddick, A. G., Sienkiewicz, M., and Woollen, J.: MERRA: NASA's Modern-Era Retrospective Analysis for Research and Applications, J. Climate, 24, 3624–3648, doi:10.1175/Jcli-D-11-00015.1, 2011.

Rosenzweig, C. and Abramopoulos, F.: Land-surface model development for the GISS GCM, J. Climate, 10, 2040–2054, doi:10.1175/1520-0442(1997)010<2040:Lsmdft>2.0.Co;2, 1997.

Sacks, W. J., Deryng, D., Foley, J. A., and Ramankutty, N.: Crop planting dates: an analysis of global patterns, Global Ecol. Biogeogr., 19, 607–620, doi:10.1111/J.1466-8238.2010.00551.X, 2010.

Schaefer, K., Collatz, G. J., Tans, P., Denning, A. S., Baker, I., Berry, J., Prihodko, L., Suits, N., and Philpott, A.: Combined simple biosphere/Carnegie-Ames-Stanford approach terrestrial carbon cycle model, J. Geophys. Res., 113, G03034, doi:10.1029/2007jg000603, 2008.

Schaefer, K., Schwalm, C. R., Williams, C., Arain, M. A., Barr, A., Chen, J. M., Davis, K. J., Dimitrov, D., Hilton, T. W., Hollinger, D. Y., Humphreys, E., Poulter, B., Raczka, B. M., Richardson, A. D., Sahoo, A., Thornton, P., Vargas, R., Verbeeck, H., Anderson, R., Baker, I., Black, T. A., Bolstad, P., Chen, J. Q., Curtis, P. S., Desai, A. R., Dietze, M., Dragoni, D., Gough, C., Grant, R. F., Gu, L. H., Jain, A., Kucharik, C., Law, B., Liu, S. G., Lokipitiya, E., Margolis, H. A., Matamala, R., McCaughey, J. H., Monson, R., Munger, J. W., Oechel, W., Peng, C. H., Price, D. T., Ricciuto, D., Riley, W. J., Roulet, N., Tian, H. Q., Tonitto, C., Torn, M., Weng, E. S., and Zhou, X. L.: A model-data comparison of gross primary productivity: results

GMDD
8, 3147–3196, 2015

from the North American Carbon Program site synthesis, J. Geophys. Res., 117, G03010, doi:10.1029/2012jg001960, 2012.

Schmidt, G. A., Ruedy, R., Hansen, J. E., Aleinov, I., Bell, N., Bauer, M., Bauer, S., Cairns, B., Canuto, V., Cheng, Y., Del Genio, A., Faluvegi, G., Friend, A. D., Hall, T. M., Hu, Y. Y., Kelley, M., Kiang, N. Y., Koch, D., Lacis, A. A., Lerner, J., Lo, K. K., Miller, R. L., Nazarenko, L., Oinas, V., Perlwitz, J., Perlwitz, J., Rind, D., Romanou, A., Russell, G. L., Sato, M., Shindell, D. T., Stone, P. H., Sun, S., Tausnev, N., Thresher, D., and Yao, M. S.: Present-day atmospheric simulations using GISS ModelE: comparison to in situ, satellite, and reanalysis data, J. Climate, 19, 153–192, doi:10.1175/Jcli3612.1, 2006.

Schmidt, G. A., Kelley, M., Nazarenko, L., Ruedy, R., Russell, G. L., Aleinov, I., Bauer, M., Bauer, S. E., Bhat, M. K., Bleck, R., Canuto, V., Chen, Y. H., Cheng, Y., Clune, T. L., Del Genio, A., de Fainchtein, R., Faluvegi, G., Hansen, J. E., Healy, R. J., Kiang, N. Y., Koch, D., Lacis, A. A., LeGrande, A. N., Lerner, J., Lo, K. K., Matthews, E. E., Menon, S., Miller, R. L., Oinas, V., Oloso, A. O., Perlwitz, J. P., Puma, M. J., Putman, W. M., Rind, D., Romanou, A., Sato, M., Shindell, D. T., Sun, S., Syed, R. A., Tausnev, N., Tsigaridis, K., Unger, N., Voulgarakis, A., Yao, M. S., and Zhang, J. L.: Configuration and assessment of the GISS ModelE2 contributions to the CMIP5 archive, J. Adv. Model. Earth Syst., 6, 141–184, doi:10.1002/2013ms000265, 2014.

Schuster, C., Estrella, N., and Menzel, A.: Shifting and extension of phenological periods with increasing temperature along elevational transects in southern Bavaria, Plant Biol., 16, 332–344, doi:10.1111/Plb.12071, 2014.

Scott, C. E., Rap, A., Spracklen, D. V., Forster, P. M., Carslaw, K. S., Mann, G. W., Pringle, K. J., Kivekäs, N., Kulmala, M., Lihavainen, H., and Tunved, P.: The direct and indirect radiative effects of biogenic secondary organic aerosol, Atmos. Chem. Phys., 14, 447–470, doi:10.5194/acp-14-447-2014, 2014.

Shindell, D. T., Pechony, O., Voulgarakis, A., Faluvegi, G., Nazarenko, L., Lamarque, J.-F., Bowman, K., Milly, G., Kovari, B., Ruedy, R., and Schmidt, G. A.: Interactive ozone and methane chemistry in GISS-E2 historical and future climate simulations, Atmos. Chem. Phys., 13, 2653–2689, doi:10.5194/acp-13-2653-2013, 2013.

Simard, M., Pinto, N., Fisher, J. B., and Baccini, A.: Mapping forest canopy height globally with spaceborne lidar, J. Geophys. Res., 116, G04021, doi:10.1029/2011jg001708, 2011.

Sitch, S., Smith, B., Prentice, I. C., Arneth, A., Bondeau, A., Cramer, W., Kaplan, J. O., Levis, S., Lucht, W., Sykes, M. T., Thonicke, K., and Venevsky, S.: Evaluation of ecosystem dynamics,

GMDD
8, 3147–3196, 2015

plant geography and terrestrial carbon cycling in the LPJ dynamic global vegetation model, Global Change Biol., 9, 161–185, doi:10.1046/J.1365-2486.2003.00569.X, 2003.
Sitch, S., Cox, P. M., Collins, W. J., and Huntingford, C.: Indirect radiative forcing of climate change through ozone effects on the land-carbon sink, Nature, 448, 791–794, doi:10.1038/Nature06059, 2007.
Sitch, S., Friedlingstein, P., Gruber, N., Jones, S. D., Murray-Tortarolo, G., Ahlström, A., Doney, S. C., Graven, H., Heinze, C., Huntingford, C., Levis, S., Levy, P. E., Lomas, M., Poulter, B., Viovy, N., Zaehle, S., Zeng, N., Arneth, A., Bonan, G., Bopp, L., Canadell, J. G., Chevallier, F., Ciais, P., Ellis, R., Gloor, M., Peylin, P., Piao, S. L., Le Quéré, C., Smith, B., Zhu, Z., and Myneni, R.: Recent trends and drivers of regional sources and sinks of carbon dioxide, Biogeosciences, 12, 653–679, doi:10.5194/bg-12-653-2015, 2015.
Spitters, C. J. T.: Separating the diffuse and direct component of global radiation and its implications for modeling canopy photosynthesis Part II. Calculation of canopy photosynthesis, Agr. Forest Meteorol., 38, 231–242, doi:10.1016/0168-1923(86)90061-4, 1986.
Stephenson, N. L. and van Mantgem, P. J.: Forest turnover rates follow global and regional patterns of productivity, Ecol. Lett., 8, 524–531, doi:10.1111/J.1461-0248.2005.00746.X, 2005.
Sugiura, D. and Tateno, M.: Optimal leaf-to-root ratio and leaf nitrogen content determined by light and nitrogen availabilities, Plos One, 6, e22236, doi:10.1371/journal.pone.0022236, 2011.
Thornton, P. E., Lamarque, J. F., Rosenbloom, N. A., and Mahowald, N. M.: Influence of carbon-nitrogen cycle coupling on land model response to CO_2 fertilization and climate variability, Global Biogeochem. Cy., 21, Gb4018, doi:10.1029/2006gb002868, 2007.
Unger, N.: Global climate impact of civil aviation for standard and desulfurized jet fuel, Geophys. Res. Lett., 38, L20803, doi:10.1029/2011gl049289, 2011.
Unger, N.: Isoprene emission variability through the twentieth century, J. Geophys. Res., 118, 13606–13613, doi:10.1002/2013jd020978, 2013.
Unger, N.: Human land-use-driven reduction of forest volatiles cools global climate, Nat. Clim. Change, 4, 907–910, doi:10.1038/Nclimate2347, 2014a.
Unger, N.: On the role of plant volatiles in anthropogenic global climate change, Geophys. Res. Lett., 41, 8563–8569, doi:10.1002/2014gl061616, 2014b.
Unger, N. and Yue, X.: Strong chemistry–climate feedbacks in the Pliocene, Geophys. Res. Lett., 41, 527–533, doi:10.1002/2013gl058773, 2014.

GMDD
8, 3147–3196, 2015

Unger, N., Harper, K., Zheng, Y., Kiang, N. Y., Aleinov, I., Arneth, A., Schurgers, G., Amelynck, C., Goldstein, A., Guenther, A., Heinesch, B., Hewitt, C. N., Karl, T., Laffineur, Q., Langford, B., A. McKinney, K., Misztal, P., Potosnak, M., Rinne, J., Pressley, S., Schoon, N., and Serça, D.: Photosynthesis-dependent isoprene emission from leaf to planet in a global carbon-chemistry-climate model, Atmos. Chem. Phys., 13, 10243–10269, doi:10.5194/acp-13-10243-2013, 2013.

Val Martin, M., Heald, C. L., and Arnold, S. R.: Coupling dry deposition to vegetation phenology in the Community Earth System Model: implications 3 for the simulation of surface O_3, Geophys. Res. Lett., 8, 2988–2996, doi:10.1002/2014GL059651, 2014.

Vitasse, Y., Delzon, S., Dufrene, E., Pontailler, J. Y., Louvet, J. M., Kremer, A., and Michalet, R.: Leaf phenology sensitivity to temperature in European trees: do within-species populations exhibit similar responses?, Agr. Forest Meteorol., 149, 735–744, doi:10.1016/J.Agrformet.2008.10.019, 2009.

von Caemmerer, S. and Farquhar, G. D.: Some relationships between the biochemistry of photosynthesis and the gas-exchange of leaves, Planta, 153, 376–387, 1981.

Weedon, G. P., Balsamo, G., Bellouin, N., Gomes, S., Best, M. J., and Viterbo, P.: The WFDEI meteorological forcing data set: WATCH Forcing Data methodology applied to ERA-Interim reanalysis data, Water Resour. Res., 50, 7505–7514, doi:10.1002/2014wr015638, 2014.

White, M. A., Thornton, P. E., and Running, S. W.: A continental phenology model for monitoring vegetation responses to interannual climatic variability, Global Biogeochem. Cy., 11, 217–234, doi:10.1029/97gb00330, 1997.

Wittig, V. E., Ainsworth, E. A., and Long, S. P.: To what extent do current and projected increases in surface ozone affect photosynthesis and stomatal conductance of trees? A meta-analytic review of the last 3 decades of experiments, Plant Cell Environ., 30, 1150–1162, doi:10.1111/J.1365-3040.2007.01717.X, 2007.

Yienger, J. J. and Levy, H.: Empirical-model of global soil-biogenic NO_x emissions, J. Geophys. Res., 100, 11447–11464, doi:10.1029/95jd00370, 1995.

Yue, X. and Unger, N.: Ozone vegetation damage effects on gross primary productivity in the United States, Atmos. Chem. Phys., 14, 9137–9153, doi:10.5194/acp-14-9137-2014, 2014.

Yue, X., Unger, N., Keenan, T. F., Zhang, X., and Vogel, C. S.: Probing the past 30-year phenology trend of US deciduous forests, submitted, 2015a.

Yue, X., Unger, N., and Zheng, Y.: Distinguishing the drivers of trends in land carbon fluxes and biogenic emissions over the past three decades, in preparation, 2015b.

GMDD
8, 3147–3196, 2015

Zaehle, S., Medlyn, B. E., De Kauwe, M. G., Walker, A. P., Dietze, M. C., Hickler, T., Luo, Y. Q., Wang, Y. P., El-Masri, B., Thornton, P., Jain, A., Wang, S. S., Warlind, D., Weng, E. S., Parton, W., Iversen, C. M., Gallet-Budynek, A., McCarthy, H., Finzi, A. C., Hanson, P. J., Prentice, I. C., Oren, R., and Norby, R. J.: Evaluation of 11 terrestrial carbon-nitrogen cycle models against observations from two temperate free-air CO_2 enrichment studies, New Phytol., 202, 803–822, doi:10.1111/Nph.12697, 2014.

Zeng, N., Mariotti, A., and Wetzel, P.: Terrestrial mechanisms of interannual CO_2 variability, Global Biogeochem. Cy., 19, Gb1016, doi:10.1029/2004GB002273, 2005.

Zhang, X. Y., Tan, B., and Yu, Y. Y.: Interannual variations and trends in global land surface phenology derived from enhanced vegetation index during 1982–2010, Int. J. Biometeorol., 58, 547–564, doi:10.1007/S00484-014-0802-Z, 2014.

Zhao, M. S. and Running, S. W.: Drought-induced reduction in global terrestrial net primary production from 2000 through 2009, Science, 329, 940–943, doi:10.1126/Science.1192666, 2010.

Zhao, M. S., Heinsch, F. A., Nemani, R. R., and Running, S. W.: Improvements of the MODIS terrestrial gross and net primary production global data set, Remote Sens. Environ., 95, 164–176, doi:10.1016/J.Rse.2004.12.011, 2005.

Zheng, Y., Unger, N., Barley, M., and Yue, X.: Relationships between photosynthesis and formaldehyde as a probe of isoprene emission, submitted, 2015.

Zhu, Z. C., Bi, J., Pan, Y. Z., Ganguly, S., Anav, A., Xu, L., Samanta, A., Piao, S. L., Nemani, R. R., and Myneni, R. B.: Global data sets of Vegetation Leaf Area index (LAI)3g and Fraction of Photosynthetically Active Radiation (FPAR)3g derived from Global Inventory Modeling and Mapping Studies (GIMMS) Normalized Difference Vegetation Index (NDVI3g) for the period 1981 to 2011, Remote Sens.-Basel, 5, 927–948, doi:10.3390/Rs5020927, 2013.

GMDD
8, 3147–3196, 2015

Table 1. Photosynthetic and allometric parameters for the vegetation model.

PFT *	TDA	GRAC3	GRAC4	SHR	DBF	ENF	EBF	CROC3	CROC4
Carboxylation	C_3	C_3	C_4	C_3	C_3	C_3	C_3	C_3	C_4
V_{cmax25} ($\mu mol\,m^{-2}\,s^{-1}$)	33	43	24	38	45	43	40	40	40
m	9	9	5	9	9	9	9	11	5
b ($mmol\,m^{-2}\,s^{-1}$)	2	2	2	2	2	2	2	8	2
a_{wl} ($kg\,C\,m^{-2}$)	0.1	0.005	0.005	0.1	0.95	0.85	0.95	0.005	0.005
b_{wl}	1.667	1.667	1.667	1.667	1.667	1.667	1.667	1.667	1.667
σ_l ($kg\,C\,m^{-2}\,LAI^{-1}$)	0.05	0.025	0.05	0.05	0.0375	0.1	0.0375	0.025	0.05
n_0 ($kg\,N\,[kg\,C]^{-1}$)	0.06	0.073	0.06	0.06	0.046	0.033	0.046	0.073	0.06
n_{rl}	0.5	1	1	0.5	0.5	0.75	0.5	1	1
n_{wl}	0.1	1	1	0.1	0.1	0.1	0.1	1	1
r_g	0.2	0.2	0.2	0.2	0.2	0.2	0.2	0.2	0.2
LAI_{min}	1	1	1	1	1	1	1	1	1
LAI_{max}	3	3	3	3	9	5	9	3	3
γ_r $(360\,days)^{-1}$	0.5	0.75	0.75	0.5	0.75	0.25	0.75	0.75	0.75
γ_w $(360\,days)^{-1}$	0.1	0.2	0.2	0.1	0.015	0.01	0.015	0.2	0.2
H_0 (m)	1	0.8	1.3	1	19	16.5	19	0.8	1.3

* Plant functional types (PFTs) are tundra (TDA), C_3 grassland (GRAC3), C_4 savanna/grassland (GRAC4), shrubland (SHR), deciduous broadleaf forest (DBF), evergreen needleleaf forest (ENF), evergreen broadleaf forest (EBF), and C_3 / C_4 cropland (CROC3/CROC4).

GMDD
8, 3147–3196, 2015

Table 2. Phenological parameters for the vegetation model.

Variables	Description	Units	Value	Reference
T_b	Base temperature for budburst forcing	°C	5	Murray et al. (1989)
a	Parameters for budburst threshold G_b	Degree day	−110	Calibrated (Y2015)
b	Parameters for budburst threshold G_b	Degree day	550	Calibrated (Y2015)
r	Parameters for budburst threshold G_b	Dimensionless	−0.01	Murray et al. (1989)
L_g	Growing length	Degree day	380	Calibrated (Y2015)
T_s	Base temperature for senescence forcing	°C	20	Dufrene et al. (2005)
F_s	Threshold for leaf fall	Degree day	−140	Calibrated (Y2015)
L_f	Falling length	Degree day	410	Calibrated (Y2015)
P_x	Daylength threshold for leaf fall	Minutes	695	White et al. (1997)
P_i	Daylength threshold for full dormancy	Minutes	585	Calibrated (Y2015)
T_d	Threshold for drought phenology	°C	12	Calibrated (Fig. 2)
β_{min}	Lower threshold of drought limit for shrub	Dimensionless	0.4	Calibrated (Fig. S1)
β_{max}	Upper threshold of drought limit for shrub	Dimensionless	1	Calibrated (Fig. S1)
ST_b	Base soil temperature for budburst forcing	°C	0	White et al. (1997)
SG_b	Threshold for budburst with soil temperature	Degree day	100	Calibrated
SL_g	Growing length with soil temperature	Degree day	100	Calibrated
ST_s	Base soil temperature for senescence forcing	°C	10	Calibrated
SF_s	Threshold for leaf fall with soil temperature	Degree day	−80	Calibrated
SL_f	Falling length with soil temperature	Degree day	100	Calibrated
β_{min}	Lower threshold of drought limit for herbs	Dimensionless	0.3	Calibrated (Fig. S1)
β_{max}	Upper threshold of drought limit for herbs	Dimensionless	0.9	Calibrated (Fig. S1)

GMDD
8, 3147–3196, 2015

Table 3. Summary of carbon fluxes and ozone vegetation damage in different domains.

Regions	Amazon	North America	Central Africa	Europe	East Asia	Indonesia	Global
GPP ($PgCa^{-1}$)	33.4	12.3	25.7	11.5	17.9	6.7	124.6
NPP ($PgCa^{-1}$)	15.5	7.5	12.1	7.3	10.3	2.9	65
NEE ($PgCa^{-1}$)	−0.4	−0.5	−0.3	−0.4	−0.5	−0.1	−2.5
Ra ($PgCa^{-1}$)	17.9	4.8	13.6	4.2	7.6	3.8	59.6
Rh ($PgCa^{-1}$)	15.1	7	11.8	6.9	9.8	2.8	62.5
Low ozone damage to GPP (%)	−0.9	−2.4	−1.8	−2.5	−4.3	−3	−2.1
High ozone damage to GPP (%)	−2.6	−5.8	−4.4	−6.1	−9.6	−7.3	−5
Low ozone damage to LAI (%)	−0.3	−0.5	−0.6	−0.5	−0.9	−0.8	−0.5
High ozone damage to LAI (%)	−0.8	−1.2	−1.6	−1.4	−2.4	−2.1	−1.4

GMDD
8, 3147–3196, 2015

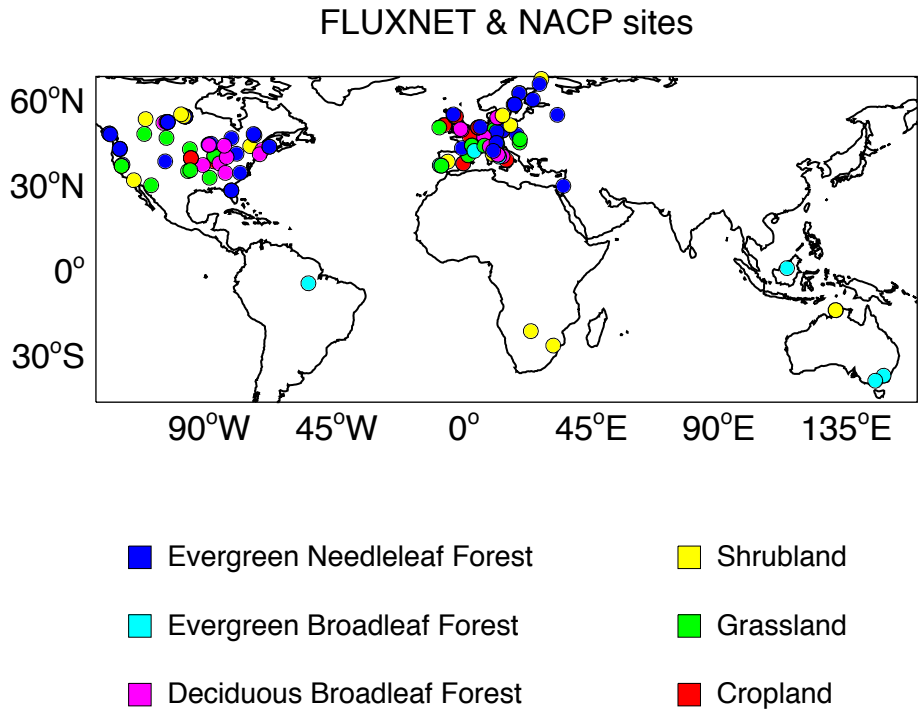

Figure 1. Distribution of 145 sites from the FLUXNET and the North American Carbon Program (NACP) network. The duplicated sites have been removed. The color indicates different land types as evergreen needleleaf forest (ENF, blue), evergreen broadleaf forest (EBF, cyan), deciduous broadleaf forest (DBF, magenta), shrubland (SHR, yellow) grassland (GRA, green), and cropland (CRO, red). "Mixed Forests" are classified as ENF, "Permanent Wetlands", "Savannas", and "Woody Savannas" as SHR. The local vegetation type at each site is described in Table S1.

GMDD
8, 3147–3196, 2015

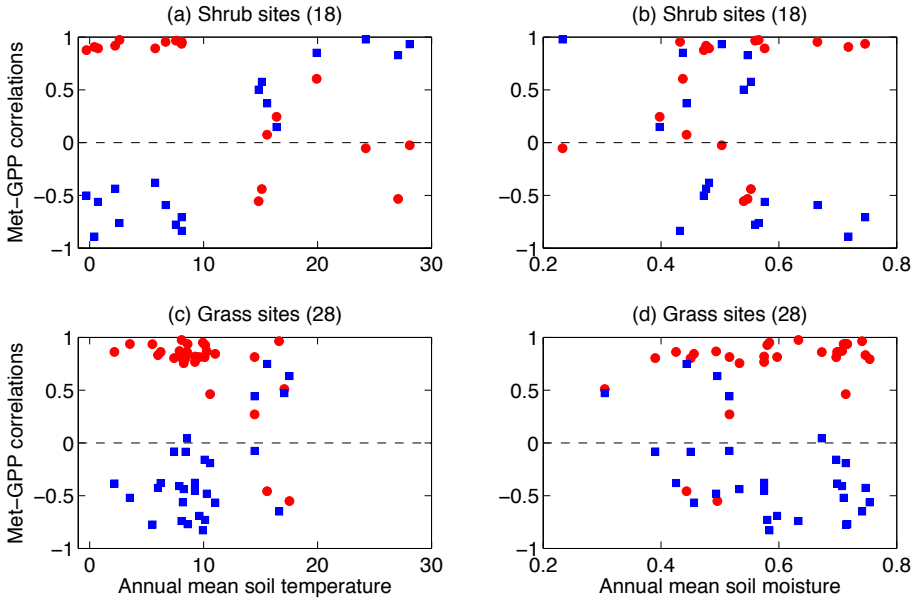

Figure 2. Correlations between monthly gross primary productivity (GPP) and soil variables at **(a, b)** shrub and **(c, d)** grass sites. For each site, we calculate correlation coefficients of GPP-soil temperature (red points) and GPP-soil moisture (blue squares). These correlation coefficients are then plotted against the annual mean **(a, c)** soil temperature (°C) or **(b, d)** soil moisture (fraction) at each site.

GMDD
8, 3147–3196, 2015

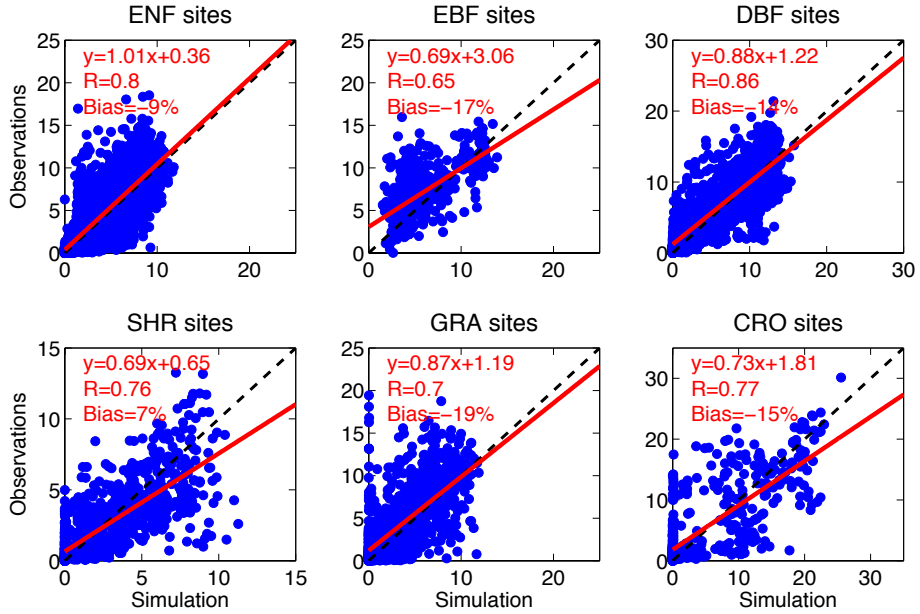

Figure 3. Comparison between observed and simulated monthly GPP from FLUXNET and NACP networks grouped by plant function types (PFTs). Each point represents the average value of one month at one site. The red lines indicate linear regression between observations and simulations. The regression fit, correlation coefficient, and relative bias are shown on each panel. The land types include evergreen needleleaf forest (ENF), evergreen broadleaf forest (EBF), deciduous broadleaf forest (DBF), shrubland (SHR), grassland (GRA), and cropland (CRO). The detailed comparison for each site is shown in Fig. S2. Units of GPP: $g C m^{-2} day^{-1}$.

GMDD
8, 3147–3196, 2015

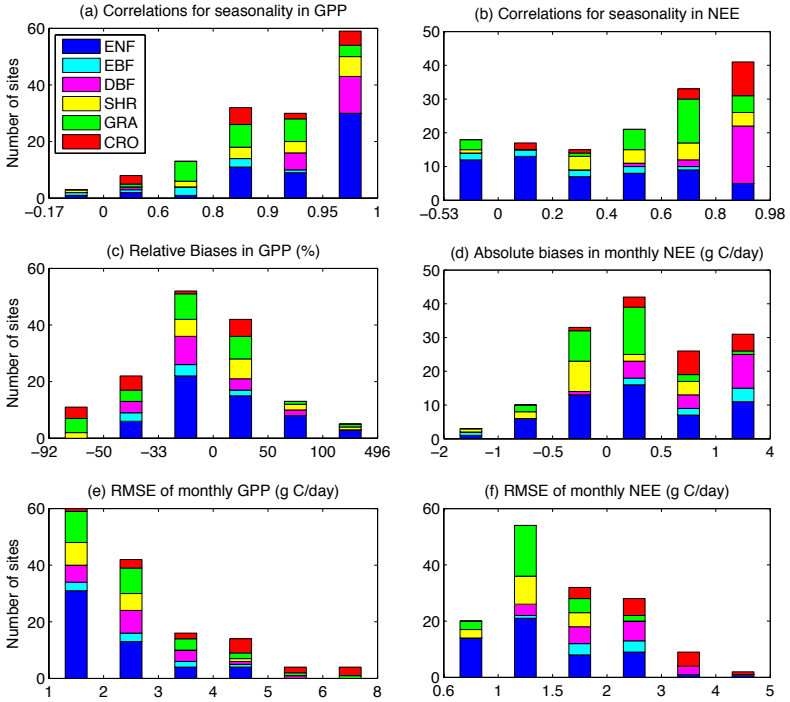

Figure 4. Histogram of **(a, b)** correlation coefficients (R), **(c, d)** biases, and **(e, f)** RMSE for monthly **(a, c, e)** GPP and **(b, d, f)** net ecosystem exchange (NEE) between simulations and observations at 145 sites. Each bar represents the number of sites where the R, bias, or RMSE of simulations fall between the specific ranges as defined by the x axis intervals. The minimum and maximum of each statistical metric are indicated as the two ends of x axis in the plots. The absolute biases instead of relative biases are shown for NEE because the long-term average NEE (the denominator) is usually close to zero at most sites. The land cover definitions are: ENF, Evergreen Needleleaf Forest; EBF, Evergreen Broadleaf Forest; DBF, Deciduous Broadleaf Forest; SHR, Shrubland; GRA, Grasslands; CRO, Croplands. Detailed comparisons at each site are shown in Figs. S2 and S4.

GMDD
8, 3147–3196, 2015

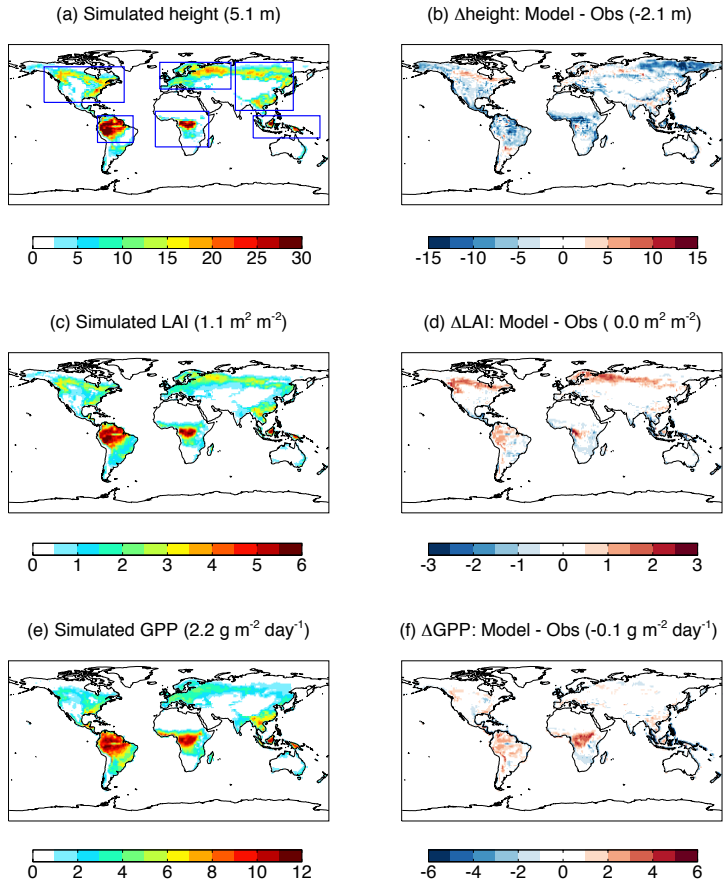

Figure 5. Simulated **(a)** tree height, **(c)** leaf area index (LAI), and **(e)** GPP and their differences relative to observations **(b, d, f)**. GPP dataset is from Jung et al. (2009). Simulations are performed with WFDEI reanalysis. Statistics are the annual average for period 1982–2011. The boxes in **(a)** represent six regions used for seasonal comparison in Fig. 6.

GMDD
8, 3147–3196, 2015

The Yale Interactive terrestrial Biosphere model

X. Yue and N. Unger

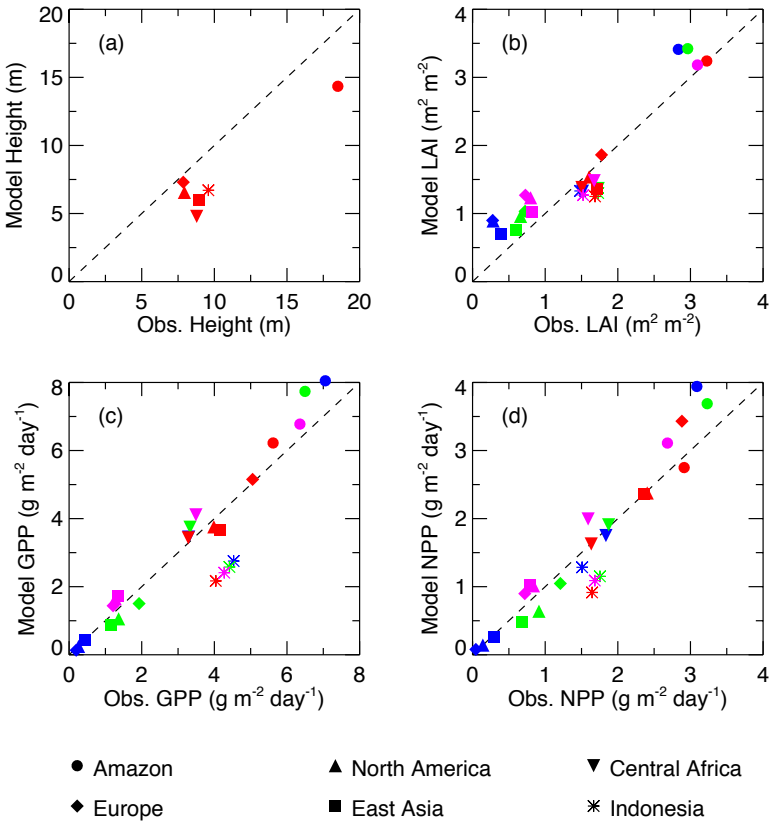

Figure 6. Comparison of annual **(a)** tree height and seasonal **(b)** LAI, **(c)** GPP, and **(d)** net primary productivity (NPP) between simulations and observations for the six regions shown in Fig. 5a. GPP dataset is from Jung et al. (2009). Values at different regions are marked using different symbols, with distinct colors indicating seasonal means for winter (blue, December–February), spring (green, March–May), summer (red, June–August), and autumn (magenta, September–November).

GMDD
8, 3147–3196, 2015

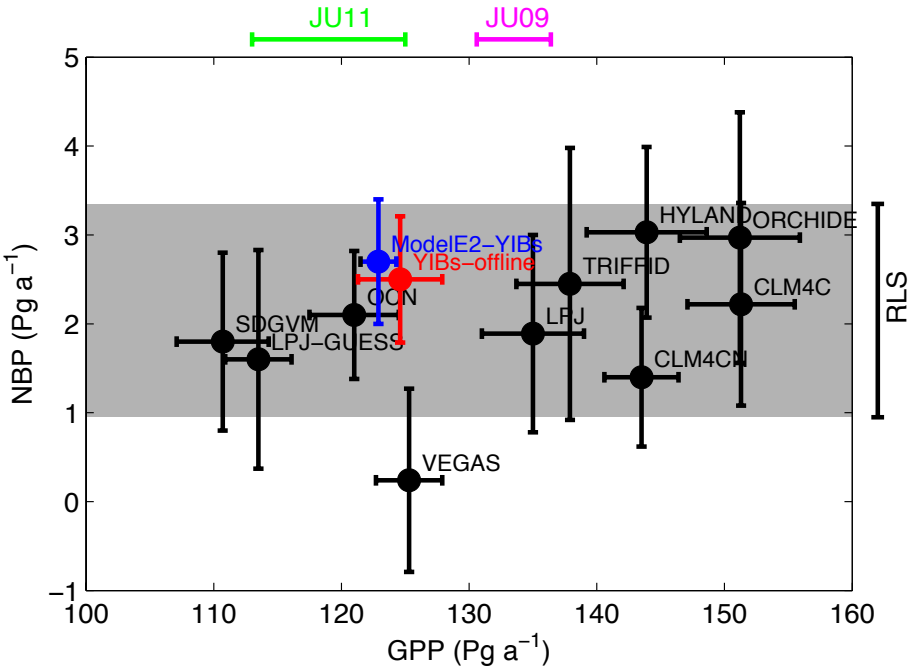

Figure 7. Comparison of simulated global GPP and net biome productivity (NBP) from (red) YIBs-offline and (blue) ModelE2-YIBs models with 10 other carbon cycle models for 1982–2008. Each black symbol represents an independent model as summarized in Piao et al. (2013). Error bars indicate the SD for interannual variability. The gray shading represents global residual land sink (RLS) calculated in Friedlingstein et al. (2010). The green line on the top represents range of GPP for 1982–2008 estimated by Jung et al. (2011) and the magenta line represents GPP for 1982–2011 from Jung et al. (2009).

GMDD
8, 3147–3196, 2015

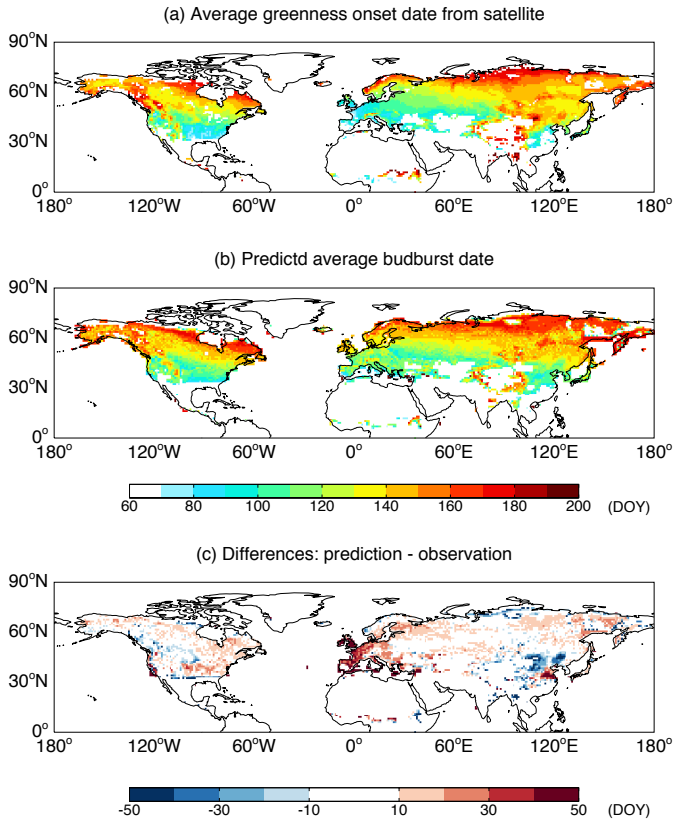

Figure 8. Comparison of simulated budburst dates in Northern Hemisphere with remote sensing. Simulated phenology in each grid square is the composite result from DBF, tundra, shrubland, and grassland based on PFT fraction and LAI in that grid box. Both simulations and observations are averaged for period 1982–2011. Results for Southern Hemisphere are not shown due to the limit coverage of deciduous forests and cold grass species.

GMDD
8, 3147–3196, 2015

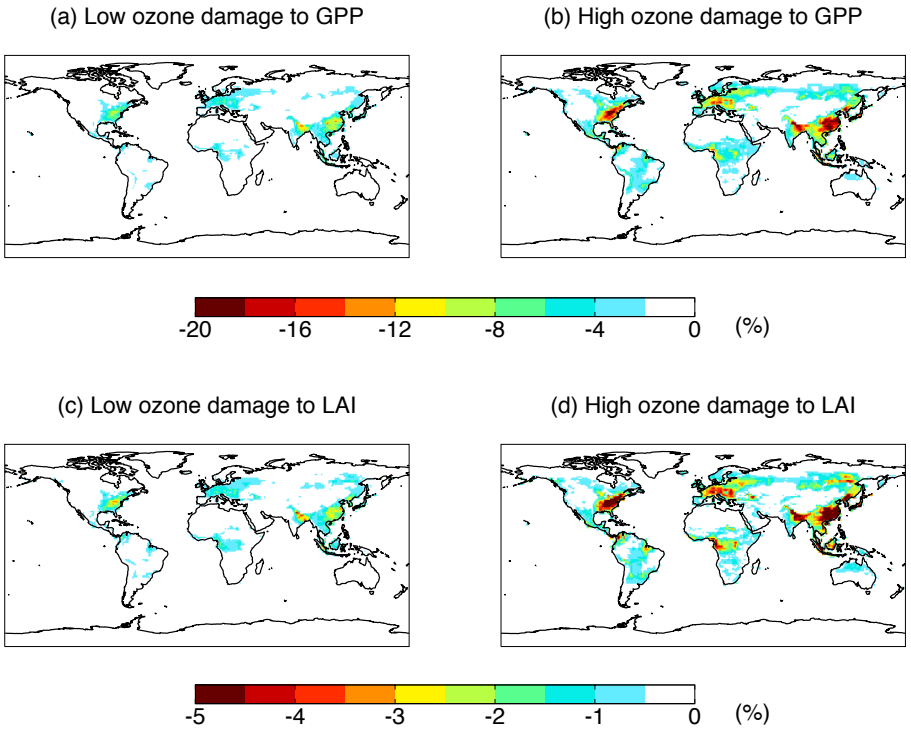

Figure 9. Percentage of ozone vegetation damage to (top) GPP and (bottom) LAI with **(a, c)** low and **(b, d)** high sensitivity. Both damages of GPP and LAI are averaged for 1982–2011. Offline surface ozone concentrations (Fig. S5) are simulated by GISS ModelE2 with climatology of the year 2000.

GMDD
8, 3147–3196, 2015